An Analysis of the MJO Guided by TRMM Rainfall Data

James J. Benedict and David A. Randall

Department of Atmospheric Science, Colorado State University

Submitted to the *Journal of the Atmospheric Sciences*

9 November 2005

Corresponding Author address: James J. Benedict, Colorado State University, Department of Atmospheric Science, 200 West Lake Street, Fort Collins, CO, 80523-1371. E-mail: jim@atmos.colostate.edu

Abstract

The Madden-Julian Oscillation (MJO), an eastward-propagating equatorial disturbance most active during the boreal winter, dominates atmospheric intraseasonal variability in the tropical Eastern Hemisphere. The MJO involves cyclic patterns of suppressed convection and intense rainfall, has a period ranging from 20-100 days, and is manifested in numerous atmospheric and oceanic variables.

This study examines various dynamical and thermodynamical processes that characterize the MJO. We identify episodes of deep convection related to the MJO based on rainfall data from the Tropical Rainfall Measuring Mission (TRMM) satellite. Although broad convective envelopes are located utilizing spectrally-filtered TRMM precipitation, analyses of the features within the envelope are carried out using unfiltered versions of TRMM rainfall and ECMWF 40-year reanalysis (ERA40) dynamical fields. The events are composited and categorized based on geographic location and relative intensity.

The composited fields illustrate that, prior to the onset of deep convection, shallow cumulus and cumulus congestus clouds are actively involved in vertical *convective* transport of heat and moisture. Drying, first accomplished immediately following deep convection in the lower troposphere, is associated with an enhanced horizontal (westerly) *advective* component and may be related to mesoscale processes as discussed in Houze et al. (2000). Deep-layer subsidence drying is delayed until one to two weeks following intense rainfall. The importance of gradual lower-tropospheric heating and moistening and the vertical transport of energy and moisture are shown in a comparison of vigorous and weak MJO events. A tiered vertical structure in moisture seen in intense MJO events indicates the possible importance of stable layers and their involvement in the growing disturbance. Additionally, a comparison of the composite fields to proposed wave instability theories suggests that the localized destabiliza-

tion and discharge-recharge mechanisms are highly relevant for explaining many of the observed features of MJO evolution.

1 Introduction

The Madden-Julian Oscillation (MJO), an equatorial disturbance first noted in the early 1970s (Madden and Julian 1971, 1994), involves multiscale cloud and precipitation processes and is manifested in numerous atmospheric variables. Despite decades of research, the combination of a poor representation of this tropical wave in most current general circulation models (GCMs) and a lack of comprehensive understanding of several of its mechanisms highlights the need for continued exploration of the MJO. This report utilizes a host of observational and reanalysis datasets to focus on the precipitation, convective, and advective processes both before and after MJO-related deep convection.

A number of studies have provided valuable insights into the structure and associated physical mechanisms of the MJO. In particular, the general characteristics and lifecycle of the MJO as seen in a number of atmospheric variables have been researched [Hendon and Salby 1994, DeMott and Rutledge 1998, Maloney and Hartmann 1998, Myers and Waliser 2003, Kiladis et al. 2005 (hereafter KSH05)]. The convective and stratiform cloud and precipitation processes during the MJO's wet phase have also been investigated (Lin and Johnson 1996a,b; Houze et al. 2000; Kikuchi and Takayabu 2004). Several other studies have focused on the regional environment within which wave initiation occurs in the Indian Ocean and what related mechanisms are most important (Bladé and Hartmann 1993, Hu and Randall 1994, Kemball-Cook and Weare 2001). Lagged-regression and correlation studies based on OLR have advanced our knowledge of the vertical and temporal structure of the MJO (Woolnough et al. 2000, Sperber 2003). Straub and Kiladis (2003) examined the observed structure of convectively-coupled Kelvin waves, a type of wave that shares features with the MJO. Recently, the study of Bony and Emanuel (2005), which employed a simplified atmospheric model to examine the relationships between moisture, radiation, and convection, highlighted the importance of moist processes involved in obtaining realistic wave growth and propagation speeds of certain tropical waves. Despite this progress, we have yet to achieve a fundamental understanding of several

aspects of the MJO or a realistic simulation of intraseasonal convectively-coupled wave variability in most GCMs, clearly pointing to a need for continued observational research on this topic.

The purpose of this study is to explore certain features of the MJO—particularly the influence of shallow cumuli and cumulus congestus prior to intense convection as well as lower-tropospheric drying following heavy rainfall—using analyses of both single events and event composites based on hydrological data from the Tropical Rainfall Measuring Mission (TRMM). What role do these cloud types play as the MJO wet phase propagates eastward, and what is the timescale on which MJO-related shallow cumulus processes act? Are there differences in the nature of tropospheric heating and moistening based on the geographic location or relative intensity of the disturbance? Which mechanisms are important during the onset of low-level drying following deep convection? To answer these questions, we conduct an examination of cloud and advective processes, as gathered from reanalysis datasets, that are associated with the evolving MJO event at certain geographic locations. Composite results presented here are also compared with proposed wave instability theories including wave conditional instability of the second kind (wave-CISK; Hayashi 1970, Lindzen 1974), wind-induced surface heat exchange (WISHE; e.g., Emanuel 1987), stratiform instability (Mapes 2000), and the discharge-recharge mechanism (e.g., Bladé and Hartmann 1993).

This analysis involves a new approach to identify MJO events. Several previous studies (Hendon and Salby 1994, Maloney and Hartmann 1998, Sperber 2003, KSH05) have used linear regression techniques on datasets that are either smoothed, filtered, or indexed in some way. In the current study, spectrally filtered TRMM rainfall data is implemented solely to locate MJO-related convective envelopes, while unfiltered TRMM and ERA40 data fields are used to examine salient features *within* these envelopes. We adopt this approach in order to balance resolution with statistical clarity concerning the observed physical features, namely suppressed-phase shallow cumulus growth and lower-tropospheric drying following the heaviest rainfall.

This study is the first to examine MJO composite events based on TRMM daily rainfall using a wide range of dynamic and thermodynamic reanalysis variables. We selected rainfall as the variable on which events are based because of its strong ties to latent heating. Recently, Cho et al. (2004) used TRMM data to explore the spectral characteristics of tropical disturbances, including the MJO. Morita et al. (2005, manuscript submitted to *Dyn. Atmos. Oceans*) implemented TRMM data to examine convective and stratiform rainfall and latent heating structures of the MJO. Additionally, the TRMM-based study by Masunaga et al. (2005, manuscript submitted to *J. Atmos. Sci.*) underscores the structural complexity and importance of wave interactions within the MJO convective envelope, illustrating the usefulness of combining unfiltered data fields with guidance based on filtered signals.

The various data sources and statistical methods implemented in this study are outlined in Section 2. We display time-height composites of several fundamental variables (e.g., wind, temperature, moisture) in Section 3, and convective and advective processes related to the MJO are discussed in Section 4. Section 5 contains results from an analysis of the MJO using spatial maps and an extended data record, and in addition discusses the relevance of our results to proposed wave instability theories of the MJO. Concluding remarks are given in Section 6.

2 Data and Methodology

a. Data sources

The present study is based primarily on three data sources: TRMM, ECMWF 40-year reanalysis (ERA40), and the Moderate Resolution Imaging Spectroradiometer–Terra satellite (MODIS-Terra). Table 1 outlines the specifications of these main datasets. Appendix B lists many of the acronyms used in this report.

Our primary source for precipitation data is the TRMM satellite. The TRMM daily-averaged 1°x1° data product 3B42 is derived from a number of space-borne instruments (see Kummerow et al. 2000). TRMM's precipitation radar, the first meteorological radar designed to

operate onboard a satellite, provides a high degree of rainfall resolution and accuracy. This, combined with improved passive microwave and visible/infrared instrumentation as well as a sufficiently long data record (8+ years), offers the opportunity to study MJO events in greater detail. We employ daily-averaged 2.5°x2.5° ERA40 data to describe dynamic, thermodynamic, and radiative atmospheric states during the selected period of analysis. Although our non-precipitation results are based on ERA40 (which does not assimilate TRMM data), we are comforted by how well the ERA40 fields match up with the TRMM data. We also utilize cloud-top pressure (CTP) and temperature (CTT) from the MODIS-Terra MOD08-D3 daily-averaged 1°x1° dataset. While the accuracy of CTP in the context of multiple cloud layers is uncertain, CTP values for non-overlapping clouds above 700 hPa are accurate to within 50 hPa (see Platnick et al. 2003 and King et al. 2003 for reviews).

Several additional datasets are compared with the primary results obtained from TRMM and ERA40. Section 2c contains brief comments on these comparisons. Total precipitation from the Global Precipitation Climatology Project (GPCP; daily-averaged, 1°x1°; Huffman et al. 2001) is matched with the TRMM results. For testing purposes, an extended version of the GPCP total precipitation field (pentad-mean, 2.5°x2.5°, 1984-2004) is also utilized in combination with ERA40 data records of similar time span to identify and examine MJO events prior to the beginning of the TRMM record. We compare near-surface winds derived from QuikSCAT retrievals (JPL, 2001) with ERA40 1000 hPa winds. We also compare ERA40 OLR data with OLR retrievals from the Terra Satellite as analyzed by of the Clouds and Earth's Radiant Energy System (CERES) project.

b. Methodology

A number of statistical tools, outlined in Figure 1, are applied to the data. To isolate features that are related to the MJO, we spectrally analyze and filter TRMM total precipitation in zonal wavenumber and frequency space. Distinct convective episodes associated with the

MJO are composited based on maximum TRMM daily rainfall. From these composites, we derive additional statistical parameters, such as covariances.

Our spectral analysis of TRMM total precipitation follows the procedure of Wheeler and Kiladis (1999). Although they spectrally analyze OLR in the wavenumber-frequency domain (see their Fig. 3), our results based on TRMM precipitation are very similar (not shown). In addition to spectral analysis, we also implement spectral filtering methods to extract particular wave features from the unfiltered data. Despite the high degree of spatial and temporal variability of equatorial rainfall, we find that the larger-scale rain structures, especially when meridionally averaged, are captured reasonably well by spectral filtering over the periods and wavenumbers of interest.

In filtering the data, we isolate signals characterized by eastward-propagating waves of zonal wavenumber 1-5 and period 20-100 days. Parallel analysis is also undertaken using a 10-100 day filter. For comparison, Wheeler and Kiladis (1999) use wavenumbers 1-5 and periods 30-96 days, and Kemball-Cook and Weare (2001) effectively retain wavenumbers 1-6 and periods 10-100 days as spectral bounds appropriate for MJO filtering. Versions of the MJO-filtered dataset are used to (a) distinguish individual convective events associated with the MJO and (b) construct of a composite MJO event. We analyze the convective events using two frameworks; the first involves timeseries of meridionally averaged (10°S-5°N) rainfall anomalies at a particular longitude, and the second involves timeseries at a single gridpoint.

In the meridionally averaged framework, the MJO-filtered data is standardized based on an area-averaged mean and standard deviation (0°-360°, 10°S-10°N). This procedure brings into focus rainfall events in the highly variable tropical Indian and West Pacific Oceans, while de-emphasizing signals not associated with the MJO outside this region. We then construct Hovmöller diagrams (10°S-5°N) of the standardized data. Individual convective events are defined according to a stringent set of criteria, similar to the constraints imposed by Rui and Wang (1990). To qualify as an MJO convective episode, the standardized, filtered rainfall anomaly (R) in the Hovmöller diagram must exceed 1σ in magnitude across a 20° longitudinal extent

throughout its lifetime, which must be a minimum of 15 days. During its lifetime, R must also exceed 1.5σ at some point. The entire event must occur in the Indian or West Pacific Ocean region (50°E-180°) during the boreal non-summer months (15 September–31 May). The 17 MJO convective events that satisfy these constraints are checked by comparison with Hovmöller diagrams of unfiltered TRMM rainfall.

A goal of this paper is the exploration of the atmospheric dynamics and cloud characteristics during the developmental and decaying stages of the MJO. The processes of interest occur on spatial and temporal scales that might be eliminated by the spectral filtering. In an attempt to include these convective processes under the umbrella of the larger-scale MJO, we use the identified events based on R simply as a guide. For each event, the longitude and time of maximum R are recorded. This longitude and time become the center point of a search area using an identical Hovmöller diagram (10°S-5°N) of *unfiltered* TRMM rainfall. We devise this search area, which scans ±15° longitude and ±5 days for the maximum meridionally averaged rainfall value, based on the idea that the date and location of the filtered precipitation maximum often are not exactly collocated with their unfiltered counterparts. Following the search procedure, the resulting longitude and time of the unfiltered rainfall maximum define the *base point* (lag day 0) of the event, upon which all other variables are centered (zonal wind, specific humidity, etc.). The timeseries of these base points, a meridional averaging at fixed longitude, are analyzed from 30 days prior to rain maximum (lag -30) to 20 after rain maximum (lag +20). We then construct time-height cross-sections of all variables for all MJO events identified, and these events are composited. The final composites are converted into anomaly forms, defined as departures from the mean atmospheric state during an MJO convective event (see Appendix A). This anomaly definition mitigates problems associated with a short data record and guarantees a zero time mean for the composite span, a useful feature for later statistical analyses.

In addition to meridional averaging, we also define events based on a single gridpoint using a similar procedure. The gridpoint analysis is conducted to identify more localized features

that may be masked by meridional averaging. In identifying events, we utilize thresholds similar to those of the meridional average case, with the exception of slightly stronger σ constraints (to account for the absence of averaging) and the inclusion of a ±2° latitudinal search window.

c. Sensitivity testing and data quality

Thorough testing of the sensitivity of our results to all parameters involved in the event selection process was undertaken. The final composite results are not strongly sensitive to adjustments in the search area, but are weakly sensitive to the periods used in the initial step of filtering the raw rainfall data (20-100 days vs. 10-100 days). The maximum MJO signal using the 20-100-day filter occurred 3-4 days later than and 7°-8° east of the maximum signal as detected by the 10-100-day filter. In essence, the same eastward-propagating convective envelopes associated with the MJO are detected, but they are detected at different times and locations in their respective lifecycles. Despite this caveat, the coherent structure of the MJO convective envelope is assumed to remain nearly identical given a change of only a few days or a few degrees of longitude. Nonetheless, we must note that some differences do exist.

Testing of the data quality revealed consistency between the variables examined. The ECMWF reanalysis dataset provides complete data coverage over an area where direct observations are sparse, namely the Indian and West Pacific Oceans. This advantage is counteracted by the sensitivity of the reanalyses to parameterizations, especially in data-sparse areas. Several issues related to sensitivities of observations, data assimilation, and/or model parameterizations are listed in Table 2. Some examples of alternative datasets that might satisfy the requirements of the current study in terms of spatial and temporal domain are included in Table 2.

The MJO event composite for the meridional average case did not change significantly when daily 1°x1° GPCP precipitation data was substituted for the TRMM data. The temporal correlation between these two datasets for the time span examined (1998-2004) is at least 0.9 for most equatorial warm-ocean areas. Composited near-surface winds from QuikSCAT and ERA40

matched up very well, with a correlation of 0.96 for composited zonal winds (> 95% significance). Compared to the MJO event composite based on CERES OLR, ERA40 tended to underestimate the magnitude of the negative OLR anomaly between days 0 and +7 by ~10-15 Wm^{-2}. Overall, however, OLR values from the CERES project (Terra satellite) displayed qualitative similarity with ERA40 OLR composites, yielding a temporal correlation of 0.92 (>95% significance).

3 Results and Discussion I: Composites of Basic Variables

The present study analyzes a host of non-precipitation variables from the ECMWF 40-year reanalysis dataset. Several previous studies have suggested that analyses of synoptic- and mesoscale tropical disturbances using non-precipitation ECMWF reanalysis variables provides acceptable results. Lin and Johnson (1996a,b), in their summary of meteorological results from TOGA COARE, found that ocean-atmosphere evaporative fluxes and lower-tropospheric moisture values from the ECMWF reanalysis agreed relatively well with direct measurements from the COARE region. Straub and Kiladis (2003) analyzed convectively-coupled Kelvin waves in the tropical West Pacific and found that, overall, the ECMWF reanalysis successfully depicted vertical structures of temperature, moisture, and zonal wind.

MJO events for the meridional average and gridpoint frameworks are displayed in Figure 2. Of the 17 (13) MJO events detected by the TRMM satellite for the meridional (gridpoint) averaged case, 11 (9) are contained in ERA40 and 13 (9) in the MODIS dataset. The locations of peak convection occur across a range of geographic regions, from the central Indian Ocean to the International Date Line. None of the gridpoint events occur directly over land masses, and any events with unreasonable or unphysical data values are discarded.

The meridionally average composite time-height plots for selected variables are presented in Figures 3 and 4. Zonal wind cross-sections (not shown) indicate the expected transition from surface easterlies prior to intense rain to westerlies following maximum rain. The vertical

velocity profile (not shown) suggests weak upward motion in the lower troposphere 5-15 days prior to deep convection.

The profile of specific humidity (q'; Fig. 3a) indicates that prior to intense convection, anomalously dry air is observed during the suppressed phase of the MJO throughout much of the troposphere. Beginning around day -20, there is a tendency for weak, shallow moistening to develop below 900 hPa, possibly due to the collective effect of shallow convective clouds. Positive moisture anomalies deepen from 900 hPa to higher than 500 hPa between days -15 and -10. This progressive moistening coexists with weak rising motion (not shown) and convection (see Section 4b). Low-level drying (800-925 hPa) begins on day 0 and expands vertically up to the 650 hPa level by day +7. A slight decrease in relative humidity (not shown) accompanies this drop in q'. After this time, most of the troposphere abruptly returns to the anomalously dry state.

Variations in temperature (T') are presented in Fig. 3b. At the time of maximum rainfall, much of the middle and upper troposphere is anomalously warm with a peak temperature perturbation of 0.9 K in the 300-400 hPa layer. Simultaneously, cool anomalies occur below 550 hPa and near the tropopause level. The structure of the low-level cooling shown in Fig. 3b closely matches previous results based on radiosonde data (Lin and Johnson 1996a, Straub and Kiladis 2003), and probably arises from latent cooling of air within downdrafts (Reed and Recker, 1971) and the evaporation of stratiform precipitation (Houze, 1982). Between days -15 and -10, steady increases in low-level q' and T', and the presence of shallow convection (see Section 4b), support the view that shallow cumuli and their associated moistening and latent heat release play a role in preconditioning the atmosphere for later intense convection through destabilization (Kemball-Cook and Weare 2001, Straub and Kiladis 2003).

The MODIS-derived CTP (Figure 4a) and solar absorption at the surface (SSA'; Fig. 4b, dashed line) suggest a distinct temporal asymmetry, with a gradual decrease in both variables prior to the wet phase followed by a rapid return to the background state afterward. SST' (Fig. 4b, solid line) generally rises between days -30 and -11 during which time $SSA' > 0$, suggest-

ing less cloud coverage, weak ocean surface mixing, and minimal rainfall. SST' declines as deeper convection develops and reaches a minimum during the westerly wind burst (WWB; Lin and Johnson 1996a) 1-2 weeks following maximum rainfall.

Profiles of q', anomalous surface latent heat flux ($SLHF'$), and composite rainfall for the gridpoint framework are displayed in Figure 5. Outside of days -5 to +5, the gridpoint and meridionally averaged rain profiles are very similar (4-8 mm/day), but rainfall amounts are considerably higher near day 0 for the gridpoint case. Though noisier due to fewer events composited and less spatial averaging, the gridpoint case shares the same features as the meridional average framework for most variables, with a gradual increase and deepening of moisture anomalies prior to intense rainfall. As in Fig. 3, evidence of weak low-level drying exists soon after the peak rainfall. The $SLHF'$ profile suggests that latent energy exchanges between the atmosphere and ocean are maximized *following* intense rainfall, which suggests that the WISHE mechanism (Emanuel 1987) does not play a dominant role in this composite MJO. A secondary peak in $SLHF'$ is seen during the time of the WWB.

Plots of meridionally averaged (solid gray), gridpoint averaged (calculated using 20-100 day filter; long dashed), and gridpoint averaged (calculated using 10-100 day filter; dotted) precipitable water perturbations (PW') appear in Figure 6. All three profiles display a similar structure: dry anomalies slowly erode toward a day-0 PW' maximum; this is followed by a fairly rapid return to below-average values. The gradual moistening prior to deep convection supports the discharge-recharge theory (Bladé and Hartmann 1993) and will be discussed in greater detail in Section 5c.

4 Results and Discussion II: MJO Processes

In this section, we turn our attention to the advective and convective processes of the heat and moisture budgets, as associated with the MJO. These mechanisms represent the effect of large-scale components and the collective effect of small-scale components, including intrusions of drier air from the subtropics and shallow cumulus transports.

a. Horizontal and vertical components of advective moisture transport

The first investigation, involving advective processes associated with the MJO, addresses the specific humidity perturbation, q'. A moisture-budget analysis is conducted by decomposing the local time rate of change of q' into its horizontal and vertical components:

$$\frac{\partial q'}{\partial t} = -\left(u\,\frac{\partial q}{\partial x}\right)' - \left(v\,\frac{\partial q}{\partial y}\right)' - \left(\omega\,\frac{\partial q}{\partial p}\right)' + S_q' - C' \qquad (1)$$

Here, S_q' and C' are the sources and sinks of q'. The contributions by S_q' and C' (evaporation and condensation, respectively) are not explicitly analyzed due to the absence of these ERA40 data on individual pressure levels.

Figure 7 depicts the combined effects of the horizontal and vertical components that contribute toward changes in q' for the meridional average case. Panel (a) displays the moderate, immediate drying brought about by the horizontal wind component between day 0 and +5. By comparison with panels (b) and (c), it is clear that this horizontal drying component has a noticeable impact on the moisture, particularly during the first three days following the peak of the wet phase and at a pressure range of 650-850 hPa. This could perhaps be evidence of a lower-tropospheric infiltration of dry air surging eastward behind the intense convection. The dry air may earlier have come from the subtropics.

Vertical advection is clearly important during the two weeks prior to intense rainfall, while post-convective drying can be parsed into immediate (horizontal) and delayed (vertical;

"subsidence") advective processes. The gridpoint results (not shown), a composite of fewer events, are less clear but lend support to the rapid horizontal and delayed vertical drying in the lower troposphere. The concept of immediate and delayed drying mechanisms in the context of tropical waves has only recently been discussed in previous studies (Kemball-Cook and Weare 2001, Sperber 2003, KSH05). Maloney and Hartmann (1998) investigate the post-convective drying processes associated with Rossby wave circulations emanating from the equatorial heat source. Our results support their findings, i.e., that drying is associated with strong lower-tropospheric westerly winds and boundary layer divergence about 10 days after the intense rainfall. We point out, however, that a more immediate drying component is seen in the reanalysis composites presented here, a small-scale feature that might not be clearly seen in the pentad-mean, bandpass-filtered data analyzed by Maloney and Hartmann (1998). This immediate drying could be partly related to the midlevel westerly inflow below the stratiform cloud decks of mesoscale tropical convective systems, as documented by Houze et al. (2000) during TOGA COARE in the West Pacific warm pool. Indeed, stratiform processes—as inferred by the vertical positioning of Q_1' and Q_2' maxima (Johnson and Young 1983, Luo and Yanai 1984)—appear to be active at the time of this drying in our results (Fig. 10a,b). However, in the present study it was found that the low-level drying associated with the horizontal wind components was most pronounced in events within the Indian Ocean (not shown), as opposed to those in the West Pacific. As Houze et al. (2000) point out, the exact nature of midlevel dry inflow hinges on the mutual interactions between mesoscale convection and the ambient dynamical fields (the forced Kelvin-Rossby wave response). Whether this interaction has a longitudinal dependence in the Tropics remains unknown.

The importance of vertical advective moistening is highlighted in the gridpoint cross-section (Figure 8; 10-100 day filtering). Between days -15 and -5, episodic vertical q' transport is noted. These "flame-like" features are generally capped near the 500 hPa level and are suggestive of the role of shallow cumuli and cumulus congestus in moistening and heating the lower troposphere, as will discussed below.

b. Convective processes

We can infer that shallow convective processes are active prior to intense MJO rainfall by analyzing the apparent convective heat source (Q_1) and apparent convective moisture sink (Q_2) (Yanai et al. 1973):

$$\begin{aligned} Q_1 &\equiv Q_R + L(c-e) - \frac{\partial}{\partial p}\,\overline{s'\,\omega'} \\ &= c_p\Big[\frac{\partial T}{\partial t} + \mathbf{v}_h \bullet \nabla_h T + \Big(\frac{p}{p_o}\Big)^{\kappa}\,\omega\,\frac{\partial \theta}{\partial p}\Big] \end{aligned} \tag{2}$$

$$\begin{aligned} Q_2 &\equiv L(c-e) + L\,\frac{\partial}{\partial p}\,\overline{q'\,\omega'} \\ &= -L\Big[\frac{\partial q}{\partial t} + \mathbf{v}_h \bullet \nabla_h q + \omega\,\frac{\partial q}{\partial p}\Big] \end{aligned} \tag{3}$$

In (2), Q_1 is a combined measure of heating by radiation (Q_R), net latent heating [$L(c-e)$], and the vertical convergence of eddy sensible heat transports. In (3), Q_2 represents the net latent heating and the vertical convergence of eddy moisture transports. The magnitude of atmospheric heating or cooling brought about by convective processes can be deduced by measuring perturbations in the heat and moisture budgets applied on large (ERA40 gridbox-sized) scales. Ideally, the budget analysis should be conducted on scales large enough to contain a collection of individual convective clouds and small enough to be only a fraction of the total cloud cluster area (Emanuel 1994), as illustrated in Figure 9. If there are nonzero residuals computed from the large-scale budget analyses [rhs of (2) and (3)], these residuals represent the effects of "subgrid-scale" convection on the larger gridbox area.

Time-height profiles of Q_1' and Q_2' (Figure 10) for the gridpoint framework indicate tropospheric cooling prior to day –15, probably due to radiation. Simultaneously, the Q_2' plot shows low-level moistening (negative values) due to surface evaporation. The key feature of Fig. 10 occurs between days -15 and -5; at this time, positive T', q', and Q_1' exist. Additionally, Q_2' shifts from moistening to drying, signifying a transition from lightly- or non-precipitating shallow clouds to deeper precipitating clouds. Together these observations indicate the presence and importance of deepening cumuli and the associated detrainment of moisture into

the dry mid-troposphere. Increased moisture in the mid- and upper-troposphere acts to decrease the efficiency of low-level radiative cooling and thus partially offsets cooling by upward motion. Using a simple atmospheric model, Bony and Emanuel (2005) show that, with a small convective time lag, the phase difference between heating and positive temperature anomalies decreases with stronger feedbacks between moisture and radiative cooling. Those authors maintain that moisture-radiation feedbacks are vital in producing more realistic wave propagation speeds and growth rates for MJO-like disturbances.

c. Driving heat and moisture variances

Wave generation, amplification, and maintenance require an energy source. In the low latitudes, the generation of eddy available potential energy (EAPE) and its conversion to eddy kinetic energy (EKE) due to localized heating and moistening fuel tropical waves. EAPE is associated with heightened T variance and is increased when $\overline{Q_1' T'} > 0$. Vertical profiles of $\overline{Q_1' T'}$ and $\overline{-Q_2' q'}$ for three stages leading up to deep convection are displayed in Figure 11.

Between days -15 and -10, an enhancement in the effectiveness of lower-tropospheric moistening by shallow cumuli, likely due to an increase in their number and coverage as evidenced by the decline in surface solar absorption (SSA'; Fig. 4), heralds the end of the suppressed (dry) phase. The more widespread coverage of shallow cumuli is reflected in the profiles of ω' (not shown), T', and q' (Fig. 10). Profiles of $\overline{Q_1' T'}$ and $\overline{-Q_2' q'}$ within this time window (dot-dashed lines in Fig. 11) suggest that radiative cooling ("1") occurs above 450 hPa. Weak radiative cooling ("2") from the top of the mid-level warm (and progressively more moist; see Fig. 10) layer also persists. Between 650 hPa and 800 hPa for days -15 to -10, detrainment from shallow cumuli has moistened and continues to moisten the layer. This observation, combined with only a minimal increase in precipitation, aids in increasing q variance at low levels ("3" in Fig. 11b). Collectively, mid- and upper-level radiative cooling, elevated SSTs, and low-level heating and moistening effectively increase CAPE, thus destabilizing the atmo-

sphere and preconditioning the region for an intensification of convection (e.g., Kemball-Cook and Weare 2001). These features lend support to the discharge-recharge theory.

Increasing coverage, intensity, and vertical growth of cumuli occur between days -10 and -5. Upward vertical motions (not shown) and positive T' and q' (Fig. 10) amplify and rapidly extend toward the upper troposphere as deep convection becomes more active. Precipitation rates gradually trend upward and are associated with warm anomalies at low levels. At this time, near-surface (upper-level) u' becomes more negative (positive; not shown). Several interesting features are apparent in the day -10 to -5 covariance profiles (dashed lines in Fig. 11). Although there is little activity above 400 hPa, low-level convective heating of warm, moist air ("4", $\overline{Q_1' T'} > 0$) below 775 hPa drives T variance and aids wave growth and intensification of convective clouds. Simultaneously, the enhanced condensation rate (i.e., rainfall production) by growing cumuli dries the atmosphere below 800 hPa ("5" in Fig. 11b), while at the same time clouds continue to detrain moisture into the overlying dry layer near 500 hPa, preparing the atmosphere for deep convection.

5 Extended Analyses and Interpretation

a. Single event map sequence

The composite cross-sections presented thus far provide detailed information about the temporal and vertical variability of an MJO event. To gain a flavor of the horizontal spatial characteristics of the tropical disturbance, we present map sequences (Figure 12) of rainfall, low-level winds, and moisture for a single MJO event centered at 2.5°S, 67.5°E (*origin point*; circled in each Fig. 12 frame) with corresponding total rainfall maximum of 80.1 mm on 21 October 1998 (lag 0). This event shares many of the characteristics seen in the composite map sequence (not shown), but is unique in that it appears to capture the initiation of an MJO event in the equatorial west-central Indian Ocean.

The development of intense rainfall at the origin point appears to be associated with a strengthening of the Somali Jet and a slow migration of an anticyclonic gyre ("A" in Fig. 12) from southern India to its location just west of the origin point on day 0. The northerly flow on the east side of the anticyclonic gyre encounters an increasingly stronger southeasterly flow near the origin point, greatly enhancing low-level convergence. An area of precipitation rapidly blossoms directly over the origin point on day -3 (not shown) and strengthens to its maximum intensity on day 0. For this event, intense rainfall developed *in situ* and did not propagate toward the origin point from the west, making this a fairly unique case among the events examined in this study. Also at this time, a dry air mass is seen over southern India and the Arabian Sea.

After day 0, maximum rainfall shifts eastward to near 100°E by day +5. Inspection of $q'_{775\,\mathrm{hPa}}$ (Fig. 12) and $\omega'_{775\,\mathrm{hPa}}$ (not shown) between days 0 and +5 indicates that a rapid drying trend at 775 hPa is associated with westerly winds but not sinking motion, further supporting the importance of the initial low-level advection of dry air by horizontal westerly wind anomalies as discussed in Section 4a. Another important feature noted in $q'_{775\,\mathrm{hPa}}$ is the merging of dry air masses to the west of the origin point. The pocket of dry air at 775 hPa seen on day +5 (Fig. 12b, center 10°N, 55°E) drifts southward, eventually merging with an expanding dry air mass centered near 7.5°S, 55°E. Following the air mass merger, this very dry air and attendant subsidence are advected toward the origin point on day +12. Daily maps of PW' (not shown) clearly display the merging of independent, dry air masses of subtropical origin at approximately 10° west of the origin point. Following the merging of the air masses, lower-tropospheric dry air is advected to the origin point 2-4 days later. The dry air mass is associated with $OLR' > 0$, $PW' < 0$, $q' < 0$ at and below 600 hPa, and $\omega' > 0$ (sinking) below 600 hPa (not shown).

b. The MJO over an extended record: Geographical and strength distinctions

Additional analyses are conducted to investigate the robustness of MJO events over a longer data record using an alternative precipitation dataset. Implementing procedures similar to those outlined in Section 2b, with slight modifications, MJO events are defined based on pentad-mean GPCP rainfall. The composite fields for all 46 MJO events detected during the period of analysis discussed above (1984-2002) match up reasonably well with the composites based on daily-averaged TRMM rainfall (1998-2004) but are notably smoother. Owing to the larger data sample, anomalies in this context are calculated as the departure from the linearly detrended, calendar-day means and are similar to those discussed in Appendix A.

Results from the longer data record composites support the findings in Sections 4 and 5a, and also provide an opportunity to examine differences of the MJO vertical-temporal structure based on geography and event strength. Geographically, MJO events are broken up by region: Indian Ocean (IO; 50°-100°E; 16 events), Maritime Continent (MC; 100°-145°E; 13 events), TOGA COARE (150°-160°E, 8 events), and West Pacific (WP; 150-180°E; 17 events). WP events, as measured by maximum day-0 rainfall, tend to be more intense than those in other regions. The GPCP composites suggest that the suppressed phase of the MJO is most notable in the IO, where comparatively low rain amounts are observed when deep convection is inactive. The range of rainfall amounts is least for MC events, likely due to land surface heating and diurnal convection even during the suppressed phase.

Cross-sections of u' (Figure 13) indicate that wind structures in the IO are more vertically stacked than in regions farther east. Low-level easterly anomalies prior to deep convection tend to be stronger in the IO as well, with a notably weaker signal for WP events. Aside from the pronounced westward vertical tilt, the u' westerly maximum for MC events is delayed by two pentads and is higher (650 hPa) when compared to IO and WP events, which have a day +5 peak at 750 hPa. This u' delay and upward shift, as well as several other general features of

the vertical-temporal structure, are qualitatively similar to those found in previous studies (e.g., KSH05).

Plots of T' for the MJO regional analysis (not shown) provide an interesting comparison with the results of KSH05. Our results for the MC case closely match the T' structure at Medan (KSH05 Fig. 8c), a west Indonesian island location, where cool anomalies below 800 hPa and above 600 hPa with a warm layer in between precede deep convection. In contrast, WP events display a more extended period of warm anomalies throughout the sub-600 hPa level prior to intense rainfall, consistent with KSH05 and indicative of a gradual vertical progression of warmth (and moisture) into the middle and upper levels as deeper convective clouds develop.

Moisture profiles (Figure 14) reveal several geographic differences. Composites of ERA40 q' for IO events display a prolonged period (day -25 to -10) of elevated moisture levels below 750 hPa with dry anomalies aloft, followed by an abrupt rise of moisture into the mid-troposphere after day -10. MC events are associated with a more gradual rise in q' with time and a slightly earlier onset of low-level drying following intense rain. Moisture profiles from the COARE region (Fig. 14c) are similar to WP events and depict the development of a $q' > 0$ tongue near the surface on day -20, and then evolving into a deeper layer of positive anomalies. Additionally, mid-tropospheric positive q' following intense rainfall for COARE and WP events appears to linger approximately 2-5 days longer than IO and MC events, where a more rapid onset of strong, deep subsidence is noted. These results are generally consistent with those of Straub and Kiladis 2003 and KSH05, with the exception of the earlier appearance of a moist layer for IO events. We ascribe this difference to the fact that most events in the IO composite are located in the central or eastern IO and thus potentially share more similarities with MC events than the selected q profile at Diego Garcia (KSH05, Fig. 10a), which is in the western IO.

MJO events are also categorized into "strong" and "weak" events based on day-0 rainfall. Strong (weak) events are defined as those in which day-0 rainfall is 0.75σ greater (less) than

the mean day-0 rainfall. Of the 47 total events, 10 are classified as strong and 11 weak. This categorization of event strength might provide some insight into what features are prominent during vigorous MJO activity. It is well known that many current atmospheric GCMs lack a realistic MJO-related variance for many fields, including T' and q' (see review in Lin et al. 2005, manuscript submitted to *J. Climate*). Thus, analyzing the observed behavior of such variables before and after MJO events and comparing this behavior to GCM output might help us to understand the model's deficiencies.

Comparing composite cross-sections for the strongest and weakest events, stronger surface easterly and westerly anomalies appear before and after day 0, respectively, for the most powerful MJO events (not shown). A steep gradient of surface u' preceding maximum vertical velocity (not shown) supports the theory that boundary layer convergence, particularly involving moisture, plays a critical role in generating MJO-related convection (e.g., Maloney and Hartmann 1998, Kemball-Cook and Weare 2001).

Concerning T', strong events have more pronounced and extended lower-tropospheric warm anomalies preceding intense MJO-related rainfall (Figure 15). This warmth is confined to below 700 hPa while abnormally cooler air exists above 600 hPa prior to day -10, indicative of a more unstable atmosphere for the strongest events. Weaker events have only marginal warm anomalies, which are positioned at a higher level (550-750 hPa) and develop one pentad after those seen in the strong event composite. As tropical atmospheric warming is intimately related to cloud and radiative processes, it is likely that the contrasting behavior in T' structure between weak and robust MJO events is directly linked to cumulus activity.

Profiles of q' (Figure 16) suggest that increased levels of lower-tropospheric moisture develop earlier and are deeper for strong MJO events. The onset of $q' > 0$ for strong events (Fig. 16a) occurs near 900 hPa on day -20, followed by a secondary lobe of development at 550-700 hPa on day -15 and then gradual deepening. In weaker events (Fig. 16b), low-level moisture increases first at 850 hPa near day -15 (one pentad later than strong events) and then gradually deepens. The structural differences between the onset of $q' > 0$ seen in Fig. 16 may

play an important role in differentiating fundamental physical processes that govern generation and maintenance of MJO-related convection. The authors hypothesize that the two-tiered signal of q' reflects the position of stable layers [the trade inversion near 850 hPa and the freezing level near 550 hPa (Johnson et al. 1996, Kikuchi and Takayabu 2004)]. It is possible that the presence of these layers allows moisture to accumulate below them, thus leading to more sudden and vigorous convection and diabatic heating several days afterward. No such tiered structure exists in the weak-event composite; rather, the onset of $q' > 0$ in Fig. 16b occurs at the level where q' is a local *minimum* in Fig. 16a. What role stable layers play in MJO events—and exactly how these layers influence or are influenced by the events themselves—remains an intriguing question.

One of the most striking contrasts between strong and weak events is a lack of convective heating prior to maximum precipitation for weak events (Figure 17). Fig. 17a, the composite of vigorous MJO events, indicates that convective processes below the freezing level are active two weeks before the most intense rainfall is observed. Around this time, warm and moist anomalies (Figs. 15a and 16a, respectively) coexist with this convective heating, as do distinct upward velocity perturbations and anomalous upward moisture transport (not shown), signifying the presence of shallow cumuli and cumulus congestus clouds. We can infer from Fig. 17b that cumulus activity in weak events is far more isolated and does not precondition the atmosphere as efficiently. These results illustrate the importance of lower-tropospheric heating and moistening and destabilization of the atmosphere prior to robust MJO-related deep convection. Additionally, Fig. 17 reiterates the need for GCMs to accurately parameterize or simulate shallow cumuli and their effects on the neighboring environment in relation to the MJO.

c. Comments on statistical significance

As a brief digression, we examine issues of statistical significance. Fig. 10 indicates a very weak signal but of correct physical sign associated with general heating and moistening of the lower levels preceding deep convection. Areas of statistical significance, however, are not

present where shallow cumulus activity is anticipated. In the first five days following intense rainfall, there is evidence of rapid drying associated with the increase in horizontal winds (Fig. 7). Significance plots (not shown) suggest that this drying is statistically significant above the 90% level. There are many difficulties in applying the concepts of statistical significance to the results in this paper, mainly due to the relatively short TRMM data record. Despite these limitations, the physical results should not be completely discounted. For example, although significance is below 95% in the lower troposphere between days -10 and -5 in a plot of Q_1', active vertical moisture transport and warm, moist anomalies (Figs. 8 and 10) suggest a physical link explained by shallow convective clouds. Additionally, observational experiments such as TOGA COARE testify to the presence and importance of such shallow cloud activity (Lin and Johnson 1996b, DeMott and Rutledge 1998). Concerning post-convective drying, strong, statistically significant westerly winds occur within five days after intense rainfall and are coincident with a sharp decrease in low-level q'. Although only weak statistical significance is noted (not shown), the conclusion of rapid drying associated with increased zonal winds is not physically unreasonable.

d. Wave theories and the MJO: Interpreting the results

Over the past three decades, several theories have been proposed detailing the physical mechanisms that generate and maintain the MJO. Versions of these theories fall into four basic categories: wave-CISK, surface evaporation feedback (WISHE), stratiform instability, and the discharge-recharge mechanism. In this section, we review the results of this study to determine the degree of consistency between each proposed theory and the observations. Brief comments on the comparison between our results and those of the modeling study of Bony and Emanuel (2005) are included at the end of this subsection.

Wave-CISK involves instability that occurs as a result of "cooperation" between localized convective heating and its environmental large-scale circulation [e.g., Hayashi 1970, Lindzen 1974]. Possible evidence of wave-CISK-like processes is noted in the observation that initial

deep convection [see Fig. 10; also, vertical separation of Q_1 and Q_2 peaks indicates vigorous convection (Johnson and Young 1983, Luo and Yanai 1984)] appears to occur during and just before maximum low-level convergence as assessed by the temporal gradient of u' (not shown). It is unclear whether this convergence is a direct result of convective heating. Data with higher spatial resolution would be needed to confirm the precise relationships between convection and larger-scale low-level convergence. Below 500 hPa, near day 0, a second-mode baroclinic structure (warm-over-cold) is associated with convective heating of anomalously cool air (Fig. 10). This is inconsistent with wave-CISK theories which require a positive correlation between deep-layer warm anomalies and convective heating. From Fig. 10, deep convective heating lags low-level T' maxima by about 1-2 weeks (out of phase by more than 0.25 cycles as in Straub and Kiladis 2003). It is possible that the inferred shallow cumuli partake in a CISK-like process in which shallow heating generates weak low-level moisture convergence (Wu 2003), but this is beyond analysis with the ERA40 data (2.5°x2.5°) being used in this study. Many inconsistencies between wave-CISK theory and observations are apparent, including phase speed and vertical structure differences and global circumnavigation aspects. Overall, a direct application of the pure wave-CISK theory does not fully explain the observed disturbance.

The WISHE mechanism (e.g., Emanuel 1987) involves an instability that arises through the interaction of surface heat and moisture fluxes and large-scale wave dynamics. This theory states that eastward-propagating convective systems are maintained by increased inflow of low-level moisture, a result of surface evaporation from the ocean by anomalous easterlies. The results of this study—including the time-height composite cross-sections, spatial composites (not shown), and the single spatial event (Fig. 12)—suggest that the WISHE mechanism is not a critical component in the events examined. In general, surface fluxes and horizontal wind anomalies are stronger in the wake of the disturbance. Even in the single spatial event which occurred in the western Indian Ocean, surface fluxes (not shown) are very weak just prior to intense convection. Additionally, many events occurred in a region of climatological wester-

lies. Nonetheless, the contribution of ocean-atmosphere fluxes in the context of the MJO is certainly not negligible.

Stratiform instability arises from a positive correlation between a second-mode temperature profile and second-mode stratiform heating structure (Houze 1997, Mapes 2000). The theory of stratiform instability involves the interplay of convective and stratiform heating modes, such that reductions in convective inhibition (CIN) outweigh fluctuations in CAPE in the presence of a warm-over-cold temperature structure (Mapes 2000). The resulting deep convection and attendant convective heating profile evolve into warm-over-cold stratiform heating, in positive correlation with the original T' structure, and thus generate EAPE. Our results do not directly support pure stratiform instability theory. Instead of warm-over-cold anomalies *leading* intense convection, the MJO involves low-level warming and moistening underlying cool, dry anomalies, suggesting an increase in CAPE rather than a decrease in CIN. Additionally, Mapes (2000) found that pure stratiform instability disturbances are associated with upper-tropospheric warm anomalies positioned about 30° east of maximum convection. Our observations indicate that upper-tropospheric warm anomalies are collocated with convective heating (Q_1'; Fig. 10). The stratiform instability mechanism may play an important role between days 0 and +5 when stratiform processes appear to be most active (Fig. 10c). Perhaps this mechanism prolongs convection, and the MJO wet phase itself, by reducing CIN and regenerating or maintaining residual convection (e.g., see deep-layer $Q_1' > 0$ for days 0 to +5 in Fig. 10a).

The essence of discharge-recharge theory is that a local, gradual build-up of instability through low-level warming and moistening preconditions the atmosphere for episodes of deep convection associated with the MJO. The results of the present study compare favorably with several aspects of this gradual enhancement of instability and cumulus growth, as outlined in such papers as Bladé and Hartmann (1993), Hu and Randall (1994), and Kemball-Cook and Weare (2001). For example, time-height cross-sections of ω' (not shown), T', q' (Fig. 10), as well as profiles of CTP (Fig. 4a), SSA' (Fig. 4b), PW' (Fig. 6), and OLR' (not shown) clearly suggest a slow build-up of low-level warming, moistening, and cumulus growth.

Our results indicate that, relative to the maximum total rainfall, there is an asymmetry in timescales of the recharge and discharge phases (e.g., PW' in Fig. 6), such that convective dissipation and tropospheric drying occur more rapidly than cumulus growth and tropospheric moistening. In Figure 18, we present a schematic diagram of the discharge-recharge mechanism as seen in the reanalysis data. In terms of T' and q' (Figs. 10c and 10d), for instance, low-level warming and moistening are maximized for ~10-15 days, deep convection and precipitation processes ultimately serving to stabilize the troposphere are active for ~10 days, and suppressed convection with associated tropospheric drying are observed for ~15 days, thus yielding a 35-40-day oscillation. The timescales of these MJO stages might involve linkages between the hydrologic cycle and the ocean surface (Stephens et al. 2004) in addition to the atmospheric component as in Bladé and Hartmann (1993).

Evidence in support of *localized* destabilization via low-level warming and moistening is seen in the weak horizontal wind convergence (not shown) and the dominance of anomalous vertical moisture transport over horizontal moisture transport (Fig. 7) ~5-15 days prior to maximum rainfall. Such observations suggest that, for most of the events in the composites presented, the build-up of low-level heat and moisture is accomplished more by localized mechanisms rather than by large-scale advective processes.

A final aspect of discharge-recharge theory concerns the geographical characteristics of the MJO events analyzed and their related triggering mechanisms. In this study, most of the individual events are located in the eastern Indian and western Pacific Ocean areas (Fig. 2). We chose these locations to correspond to maximum wet phase amplitude and not wave initiation, and so it is likely that the composite results largely reflect the evolution of a (nearly) fully-developed convective envelope. Inspection of dry static stability [$\hat{\theta}' = \frac{1}{2}(\theta'_{250\,\mathrm{hPa}} - \theta'_{775\,\mathrm{hPa}})$; Fig. 19a] supports this hypothesis, showing the shape of the $\hat{\theta}'$ profile to be quite similar to a model-generated stability composite of events 90° downstream of wave initiation (Fig. 11c in Bladé and Hartmann 1993). The individual event (21 October 1998) presented in spatial map sequences in Fig. 12 occurs in the western Indian Ocean and provides some support for dis-

charge-recharge theory as interpreted by Bladé and Hartmann (1993; see their Fig. 11a). Although the signal is noisy, the $\hat{\theta}$ profile (Fig. 19b) indicates a steady decline in stability beginning near day -14, a minimum a few days prior to deep convection, and a rapid increase during the deep convection. Note the distinct differences between panels (a) and (b) of Fig. 19. The destabilization near day -5 is likely due to the observed sharp increase in $h_{1000\,\mathrm{hPa}}$ (moist static energy at 1000 hPa), while $h_{400\,\mathrm{hPa}}$ remains quite low (not shown). Additionally, the 21 October 1998 event appears to have ties to a subtropical trigger in the form of low-level convergence impinging on the Tropics as in Bladé and Hartmann (1993). Overall, the theory of localized destabilization and the discharge-recharge mechanism successfully explains many of the observed features of MJO evolution.

A recent modeling study conducted by Bony and Emanuel (2005) emphasized the importance of feedbacks between moisture anomalies with radiation and convection. Simulated planetary-scale waves were slowed to more realistic phase speeds due to a decreased effective stratification caused by less-efficient radiative cooling in the presence of moisture anomalies. Additionally, a tendency for planetary wave destabilization arises with stronger moisture-radiation feedbacks when tropospheric temperature anomalies become more in-phase with vertical velocity anomalies. The results of the present study compare favorably with these model results. In particular, the upper-right panel of their Figure 5 (Bony and Emanuel 2005) indicates that lower-tropospheric temperature perturbations lead maximum upward motion, which itself is nearly in-phase with mid- to upper-tropospheric temperature anomalies for the case of strong moisture-radiation feedback ($\alpha = 12$). This is consistent with plots of T' (Fig. 16a) from the current study, given that maximum upward motion occurs with maximum total rainfall (not shown). With stronger moisture-radiation feedbacks ($\alpha = 30$; their Figure 4), there is even better agreement between the model results and our reanalysis-based composites.

6 Concluding Remarks

This study focuses on a number of key elements that characterize the MJO. Our results suggest that reanalysis data is suitable for use in capturing the large-scale and mesoscale features of the approach and departure of the MJO convective phase. Most previous research studies utilize filtered or regressed data fields that could blur potentially important smaller-scale features such as the rapid post-convective, lower-tropospheric drying signal associated with horizontal winds, as seen in the present study. Abundant evidence of pre-deep-convective shallow cumulus activity, a physical process that could be masked by smoothing or filtering, is also noted. In general, the statistical approach implemented in analyzing certain MJO mechanisms must cater to the scale of that mechanism, which is why we use unfiltered, higher-resolution rainfall within a filtered, MJO-related convective envelope.

Our analysis highlights the importance of shallow convective heating and moistening by cumuli prior to the arrival of the intense rainfall. During the two weeks leading up to day 0, convective vertical transport of positive T' and q' in the lower troposphere and extending into the middle troposphere plays a critical role in "preconditioning" the environment for deep convection, as in Bladé and Hartmann (1993) and Kemball-Cook and Weare 2001. Near day 0, precipitation processes evolve from convective to stratiform, according to the vertical structures of Q_1' and Q_2'.

Following deep convection, we note distinct vertical and temporal drying processes. The composite results indicate that there is a tendency for the horizontal winds ($\mathbf{v}_h$) to be associated with low-level drying soon after the most intense precipitation has ended. This drying related to the initial $\mathbf{v}_h$ maximum occurs a few days earlier than the onset of deep-layer subsidence and 1-2 weeks earlier than the most intense subsidence. Previous studies, including Hendon and Salby (1994) and Maloney and Hartmann (1998), implement smoothed data fields to analyze this delayed deep-layer subsidence and drying. While the results presented here

strongly support their results, we find that a more immediate drying associated with horizontal advection may play an important role only a few days following intense rainfall. This drying, possibly linked to midlevel mesoscale inflow (Houze et al. 2000), appears to influence the vertical structure of MJO-related convection and its interaction with the ambient atmosphere.

In terms of wave theories in explaining instabilities and growth associated with the MJO, we find that the results of this study agree with the discharge-recharge hypothesis [Bladé and Hartmann 1993, Hu and Randall 1994, Kemball-Cook and Weare 2001]. Preconditioning of the atmosphere by low-level heating and moistening, a fundamental aspect of the discharge-recharge theory, is clearly seen in the results of this study. Although certain elements of generalized wave-CISK, WISHE, and stratiform instability mechanisms are noted, several inconsistencies prohibit a direct application of any one of these theories to the observed MJO.

Although research on the MJO is currently into its fourth decade, many aspects of this tropical disturbance remain unsolved. Continued exploration of the issues surrounding the MJO—including wave triggering mechanisms, extratropical connections, scale interactions, and cloud processes—is a vital step toward answering these questions.

Acknowledgements. Both TRMM rainfall and MODIS cloud data were acquired as part of NASA's Earth Science Enterprise and were obtained from the Goddard Distributed Active Archive Center. ERA40 data were obtained from the ECMWF data server. Gridded GPCP data were provided by NASA/GSFC's Laboratory for Atmospheres. QuikSCAT wind data were obtained from PO.DAAC at the NASA JPL. The CERES OLR data were obtained from the NASA Langley Research Center Atmospheric Sciences Data Center. This research project was funded by the Department of Energy Atmospheric Radiation Measurement program grant DE-FG02-02ER63370, NASA contract NNG04G125G, and National Science Foundation grant ATM-981212384.

APPENDIX A

Composite Anomaly Calculation

For all non-precipitation variables A, each defined MJO event (i) contains a timeseries of that variable at all ERA40 model pressure levels (p, 1000-200 hPa). For a fixed p, the background state $\overline{A_p}$ from which departures are calculated is:

$$\overline{A_p} = \frac{1}{T} \sum_{i=1}^{N} \sum_{j=-30}^{+20} \left(A_p^j\right)_i \tag{A1}$$

where i is the event counter, N the total number of events, j the lag day counter, and T is N multiplied by the total number of lag days for each event (51). Departures from $\overline{A_p}$ are defined as follows:

$$A_p^{j\prime} = \left(\frac{1}{N} \sum_{i=1}^{N} \left(A_p^j\right)_i \right) - \overline{A_p} \tag{A2}$$

where $A_p^{j\prime}$ is the anomaly value for each pressure level and each lag day.

APPENDIX B

List of Selected Acronyms

CERES	Clouds and the Earth's Radiant Energy System
CMAP	Climate Prediction Center (CPC) Merged Analysis of Precipitation
CIN	Convective inhibition
CTP	Cloud-top pressure
CTT	Cloud-top temperature
ERA40	ECMWF 40-year reanalysis dataset
GPCP	Global Precipitation Climatology Project
IGRA	Integrated Global Radiosonde Archive
IO	Indian Ocean
MC	Maritime Continent
MODIS	Moderate Resolution Imaging Spectroradiometer
PW	Precipitable water
SLHF	Surface latent heat flux
SSA	Solar absorption at the surface
TOGA COARE	Tropical Ocean Global Atmosphere Coupled Ocean Atmosphere Experiment
TRMM	Tropical Rainfall Measuring Mission
WP	West Pacific

REFERENCES

Bladé, I., and D. L. Hartmann, 1993: Tropical Intraseasonal Oscillations in a Simple Nonlinear Model. *J. Atmos. Sci.*, **50,** 2922-2939.

Bony, S., and K. A. Emanuel, 2005: On the Role of Moist Processes in Tropical Intraseasonal Variability: Cloud-Radiation and Moisture-Convection Feedbacks. *J. Atmos.Sci.*, **62,** 2770-2789.

Cho, H.-K., K. P. Bowman, and G. R. North, 2004: Equatorial Waves Including the Madden-Julian Oscillation in TRMM Rainfall and OLR Data. *J. Climate*, **17,** 4387-4406.

DeMott, C. A., and S. A. Rutledge, 1998: The Vertical Structure of TOGA COARE Convection. Part II: Modulating Influences and Implications for Diabatic Heating. *J. Atmos. Sci.*, **55,** 2748-2762.

ECMWF, 2003: IFS Documentation CY28r1, Part III: Dynamics and Numerical Procedures. ECMWF IFS Documentation Cycle CY28r1, Reading, UK, 38 pp., ed. 2004. [Available online at http://www.ecmwf.int/research/ifsdocs/]

ECMWF, 2003: IFS Documentation CY28r1, Part IV: Physical Processes. ECMWF IFS Documentation Cycle CY28r1, Reading, UK, 175 pp., ed. 2004. [Available online at http://www.ecmwf.int/research/ifsdocs/]

Emanuel, K. A., 1987: An Air-Sea Interaction Model of Intraseasonal Oscillations in the Tropics. *J. Atmos. Sci.*, **44,** 2324-2340.

——, 1994: *Atmospheric Convection.* Oxford University Press, 580 pp.

Hayashi, Y., 1970: A Theory of Large-Scale Equatorial Waves Generated by Condensation Heat and Accelerating the Zonal Wind. *J. Meteor. Soc. Japan*, **48,** 140-160.

Hendon, H. H., and M. L. Salby, 1994: The Life Cycle of the Madden-Julian Oscillation. *J. Atmos. Sci.*, **51,** 2225-2237.

Houze, R. A., Jr., 1982: Cloud Clusters and Large-Scale Vertical Motion in the Tropics. *J. Meteor. Soc. Japan*, **60,** 396-410.

——, 1997: Stratiform Precipitation in Regions of Convection: A Meteorological Paradox? *Bull. Amer. Meteor. Soc.*, **78,** 2179-2196.

——, S. S. Chen, D. E. Kingsmill, Y. Serra, and S. E. Yuter, 2000: Convection over the Pacific Warm Pool in relation to the Atmospheric Kelvin-Rossby Wave. *J. Atmos. Sci.*, **57,** 3058-3089.

Hu, Q., and D. A. Randall, 1994: Low-Frequency Oscillations in Radiative-Convective Systems. *J. Atmos. Sci.*, **51,** 1089-1099.

Huffman, G. J., and Coauthors, 2001: Global Precipitation at One-Degree Daily Resolution from Multisatellite Observations. *J. Hydrol.*, **2,** 36-50.

Johnson, R. H., and G. S. Young, 1983: Heat and Moisture Budgets of Tropical Mesoscale Anvil Clouds. *J. Atmos. Sci.*, **40,** 2138-2147.

——, P. E. Ciesielski, and K. A. Hart, 1996: Tropical Inversions near the 0-degC Level. *J. Atmos. Sci.*, **53,** 1838-1855.

JPL, 2001: SeaWinds on QuikSCAT Level 3 - Daily, Gridded Ocean Wind Vectors (JPL SeaWinds Project). JPL D-20335, Version 1.1, Jet Propulsion Laboratory, Pasadena, CA, 39 pp.

Källberg, P., 1998: Aspects of the Re-Analysed Climate. ECMWF Re-Analysis Project Report Series #2. ECMWF, Reading, UK, 96 pp. [Available online at http://www.ecmwf.int/publications/library/do/references/list/191]

Kemball-Cook, S. R., and B. C. Weare, 2001: The Onset of Convection in the Madden-Julian Oscillation. *J. Climate*, **14,** 780-793.

Kikuchi, K., and Y. Takayabu, 2004: The Development of Organized Convection Associated with the MJO during TOGA COARE IOP: Trimodal Characteristics. *Geophys. Res. Lett.*, **31,** L10101.

Kiladis, G. N., K. H. Straub, and P. T. Haertel, 2005: Zonal and Vertical Structure of the Madden-Julian Oscillation. *J. Atmos. Sci.*, **62,** 2790-2809.

King, M., and Coauthors, 2003: Cloud and Aerosol Properties, Precipitable Water, and Profiles of Temperature and Water Vapor from MODIS. *IEEE Trans. Geosci. Remote Sens.*, **41,** 442-458.

Kummerow, C., and Coauthors, 2000: The Status of the Tropical Rainfall Measuring Mission (TRMM) after Two Years in Orbit. *J. Appl. Meteor.*, **39,** 1965-1982.

Lin, J.-L., and Coauthors, 2005: Tropical Intraseasonal Variability in 14 IPCC AR4 Climate Models Part I: Convective Signals. *J. Climate*, submitted.

Lin, X., and R. H. Johnson, 1996a: Kinematic and Thermodynamic Characteristics of the Flow over the Western Pacific Warm Pool during TOGA COARE. *J. Atmos. Sci.*, **53,** 695-715.

——, 1996b: Heating, Moistening, and Rainfall over the Western Pacific Warm Pool during TOGA COARE. *J. Atmos. Sci.*, **53,** 3367-3383.

Lindzen, R. S., 1974: Wave-CISK in the Tropics. *J. Atmos. Sci.*, **31,** 156-179.

Luo, H., and M. Yanai, 1984: The Large-Scale Circulation and Heat Sources over the Tibetan Plateau and Surrounding Areas during the Early Summer of 1979. Part II: Heat and Moisture Budgets. *Mon. Wea. Rev.*, **112,** 966-989.

Madden, R. A., and P. R. Julian, 1971: Detection of a 40-50 Day Oscillation in the Zonal Wind in the Tropical Pacific. *J. Atmos. Sci.*, **28,** 702-708.

——, 1994: Observations of the 40-50-Day Tropical Oscillation-A Review. *Mon. Wea. Rev.*, **122,** 814-837.

Maloney, E. D., and D. L. Hartmann, 1998: Frictional Moisture Convergence in a Composite Life Cycle of the Madden-Julian Oscillation. *J. Climate*, **11,** 2387-2403.

Mapes, B. E., 2000: Convective Inhibition, Subgrid-Scale Triggering Energy, and Stratiform Instability in a Toy Tropical Wave Model. *J. Atmos. Sci.*, **57,** 1515-1535.

Masunaga, H., T. L'Ecuyer, and C. Kummerow, 2006: An Observational Study of the Madden-Julian Oscillation. *J. Atmos. Sci.*, submitted.

Morita, J., and Y. Takayabu, S. Shige, 2005: Analysis of Rainfall Characteristics of the Madden-Julian Oscillation Using TRMM Satellite Data. *Dyn. Atmos. Oceans*, submitted.

Myers, D. S., and D. E. Waliser, 2003: Three-Dimensional Water Vapor and Cloud Variations Associated with the Madden-Julian Oscillation during Northern Hemisphere Winter. *J. Climate*, **16,** 929-950.

Platnick, S., M. King, S. Ackerman, P. Menzel, B. Baum, J. Riédi, and R. Frey, 2003: The MODIS Cloud Products: Algorithms and Examples from Terra. *IEEE Trans. Geosci. Remote Sens.*, **41,** 459-473.

Reed, R. J., and E. E. Recker, 1971: Structure and Properties of Synoptic-Scale Wave Disturbances in the Equatorial Western Pacific. *J. Atmos. Sci.*, **28,** 1117-1133.

Rui, H., and B. Wang, 1990: Development Characteristics and Dynamic Structure of Tropical Intraseasonal Convection Anomalies. *J. Atmos. Sci.*, **47,** 357-379.

Sperber, K. R., 2003: Propagation and the Vertical Structure of the Madden-Julian Oscillation. *Mon. Wea. Rev.*, **131,** 3018-3037.

Stephens, G. L., P. J. Webster, R. H. Johnson, R. Engelen, and T. L'Ecuyer, 2004: Observational Evidence for the Mutual Regulation of the Tropical Hydrological Cycle and Tropical Sea Surface Temperatures. *J. Climate*, **17,** 2213-2224.

Straub, K. H., and G. N. Kiladis, 2003: The Observed Structure of Convectively Coupled Kelvin Waves: Comparison with Simple Models of Coupled Wave Instability. *J. Atmos. Sci.*, **60,** 1655-1668.

Wheeler, M., and G. N. Kiladis, 1999: Convectively Coupled Equatorial Waves: Analysis of Clouds and Temperature in the Wavenumber-Frequency Domain. *J. Atmos. Sci.*, **56,** 374-399.

Woolnough, S. J., J. M. Slingo, and B. J. Hoskins, 2000: The Relationship between Convection and Sea Surface Temperature on Intraseasonal Timescales. *J. Climate*, **13,** 2086-2104.

Wu, Z., 2003: A Shallow CISK, Deep Equilibrium Mechanism for the Interaction between Large-Scale Convection and Large-Scale Circulations in the Tropics. *J. Atmos. Sci.*, **60,** 377-392.

Yanai, M., S. Esbensen, and J.-H. Chu, 1973: Determination of Bulk Properties of Tropical Cloud Clusters from Large-Scale Heat and Moisture Budgets. *J. Atmos. Sci.*, **30,** 611-627.

LIST OF FIGURES

Fig. 1. Flow diagram of the MJO event selection and compositing process.

Fig. 2. (a) Map of MJO events (longitude of maximum rainfall), detected in both TRMM (red and blue) and ERA40 (red only) datasets, that make up the composite plots for the meridionally-averaged (10°S-5°N) framework. (b) As in (a) but for the individual ERA40 gridpoint cases. Green shading represents the ERA40 land-sea mask.

Fig. 3. Composite plots of (a) q' and (b) T' for the meridional average (10°S-5°N) framework. The corresponding composite TRMM rainfall timeseries is plotted below both panels. Solid red lines (dashed blue, solid green) are positive (negative, zero) departures from the MJO background state (see Appendix A). Lag days relative to maximum rain appear on the horizontal axis.

Fig. 4. (a) As is Fig. 3, but for MODIS CTP (left vertical axis) and CTT (right vertical axis). (b) As in (a) but for SST' (solid) and surface solar absorption (SSA', dashed).

Fig. 5. As in Fig. 3 but for (a) q' and (b) $SLHF'$ for the gridpoint framework.

Fig. 6. As in Fig. 3 but for PW' based on the meridional average (solid gray), gridpoint 10-100-day filter (dotted), and gridpoint 20-100-day filter (dashed) frameworks.

Fig. 7. Plots of the (a) horizontal, (b) vertical, and (c) combined (horizontal + vertical) composites of $\partial q' / \partial t$ for the meridional average framework. Contour scheme is identical to Fig. 3, except that (a) is half the interval [0.1 (g/kg)/day] of (b) and (c). Blue, red, and yellow shading indicate values <-1.0 (g/kg)/day, between +1.0 and +2.0 (g/kg)/day, and >2.0 (g/kg)/day, respectively.

Fig. 8. Composite plot of the vertical component of $\partial q' / \partial t$ for the gridpoint framework. Contours and shading scheme are identical to those used in Fig. 7.

Fig. 9. Schematic diagram illustrating tropical cloud system scale differences. The x-y map (above inset) depicts an eastward-propagating intraseasonal oscillation (ISO) organized on scales of O(1000 km). Within a single reanalysis grid cell (e.g., ERA40, 2.5°x2.5°), which itself constitutes a small area of the ISO, an ensemble of convective clouds exists. Deeper convective towers may be "connected" by stratiform or cirriform clouds associated with detrained moisture. A number of shallow cumuli (darker shading) are shadowed by the stratiform or anvil clouds and may not be detected by passive satellite sensors, while others (lighter shading) develop under a clear sky. Q_1' and Q_2' account for the contributions of the convective cloud ensemble to the larger-scale environment.

Fig. 10. Plots of (a) the apparent convective heat source Q_1', (b) apparent convective moisture sink (Q_2'; positive values are associated with drying), (c) T', and (d) q' for the gridpoint framework. The corresponding TRMM rainfall composite for this framework appears below each panel. The general contour scheme is identical to Fig. 3, with red shading representing values >5 K/day in panels (a) and (b).

Fig. 11. Vertical profiles of (a) $\overline{Q_1' T'}$ and (b) $\overline{-Q_2' q'}$ averaged over three stages leading deep convection, for the gridpoint framework. Profiles are represented by dotted (days -30 to -15), dot-dashed (days -15 to -10), and dashed (days -10 to -5) lines. Numbers indicate features that are discussed in the text.

Fig. 12. Map sequences of (a) TRMM total rainfall and anomalous 850 hPa horizontal wind ($\mathbf{v}_h'$) and (b) q' and $\mathbf{v}_h'$ at 775 hPa for the event of 21 October 1998 based on the gridpoint framework. Here, anomaly values are departures from the climatological mean (1984-2001). Lag days are to the left of each panel. Maximum wind vector and shading scale are below and to the right of the zero lag day panel, respectively. The zero lag day corresponds to the day of maximum rain at the geographical base point (2.5°S, 67.5°E, circled in each panel). Letter "A" represents an anticyclonic gyre as discussed in the text.

Fig. 13. Composite plots of u', based on the meridional-average framework, for MJO events in (a) the Indian Ocean (IO), (b) Maritime Continent (MC), (c) TOGA COARE (TC), and (d) West Pacific (WP) regions. Corresponding TRMM rain profiles appear below each panel. Solid red lines (dashed blue, solid green) are positive (negative, zero) departures from climatology (1984-2002).

Fig. 14. As in Fig. 13 but for q'.

Fig. 15. Composite plots of T', based on the meridional-average framework, for MJO events classified as "strong" and "weak" (see text). Corresponding TRMM rain profiles appear below each panel. Solid red lines (dashed blue, solid green) are positive (negative, zero) departures from climatology (1984-2002).

Fig. 16. As in Fig. 15 but for q'.

Fig. 17. As in Fig. 15 but for Q_1'. Red shading indicates heating values >5 K/day.

Fig. 18. Schematic diagram of the discharge-recharge mechanism associated with the MJO. Along the horizontal axis appears SST' [red (blue) indicates warmest (coolest) anomalies] and the lag days relative to the day of maximum rainfall (day 0). Approximate stages of the discharge-recharge process, as seen in ERA40 data, are listed below the lag days. The approximate top level of convective cloud processes is indicated by the dashed blue line, while green shading represents the general area of $q' > 0$. Light blue dots above shallower convective clouds represent moistening via detrainment, while gray dots below stratiform cloud types represent ice crystal fall-out and moistening. Convective precipitation is indicated by darker blue rain shafts, and stratiform precipitation is light blue and slightly transparent.

Fig. 19. Timeseries of (a) the composite departures of dry static stability (defined in text) from climatology (1984-2002) for the meridional average framework, and (b) total dry static stability for the MJO event of 21 October 1998 for the gridpoint framework. Corresponding timeseries of TRMM rain appear below each panel.

Table 1. Primary data sources used in this study.

	TRMM (3B42)	*ERA40*	*MODIS*
Origin/platform	Satellite (TRMM)	Observations and model forecasts	Satellite (Terra)
Horizontal resolution	1°x1°	2.5°x2.5°	1°x1°
Chosen temporal domain	1 Jan 98-28 Feb 04	1 Jan 97-31 May 02	1 Jan 98-28 Feb 04
Vertical levels	Surface	1000, 925, 850, 775, 700, 600, 500, 400, 300, 250, 200 hPa	Single level
Variables	Total precipitation	Dynamic, thermodynamic, and radiative variables	Cloud-top temperature and pressure

Table 2. A list of some ERA40 variables and their associated issues in relation to the current study. Examples of alternative datasets appear in the third column. The proposed alternative datasets are, whenever possible, independent of the ERA40 dataset (e.g., not assimilated). These alternative datasets must also be applicable to the current study in terms of spatial and temporal domains.

ERA40 variable	*ERA40 issue*	*Example(s) of alternative data sources*	*Comments*
u, v	Slightly overestimated over open tropical oceans and underestimated over isolated island locations[a].	QuikSCAT (surface winds), radiosonde datasets* (Integrated Global Radiosonde Archive; IGRA)	Composite ERA40 and QuikSCAT surface winds compare favorably; low observation density over Indian Ocean for IGRA.
ω	Constrained to model parameterizations, especially in regions of convection[b].	None applicable to current study.	
T	Slight climatological warm (cool) bias in lower (upper) tropical troposphere[a].	Radiosonde datasets* (IGRA)	Few observations over Indian Ocean for IGRA.
Moisture (q, PW)	Slight overestimation of boundary layer q due to overestimated *SLHF* and turbulent vertical moisture transport[a].	MODIS, radiosonde datasets* (IGRA)	Few observations over Indian Ocean for IGRA.
OLR	Constrained to data assimilation scheme and radiative transfer model[b].	CERES or ERBE radiances	Composite ERA40 and CERES *OLR* compare reasonably well.
SLHF	Constrained to bulk aerodynamic parameterizations, overestimated over tropical oceans due to biases in ship observations of near-surface winds[a,b].	None applicable to current study.	

[a] The review in Källberg (1998) addresses deficiencies in the 15-year ECMWF reanalysis, no such comprehensive study has yet been published for the 40-year ECMWF reanalysis.

[b] ERA40 model documentation (ECMWF 2003), Parts III and IV.

* Select radiosonde data is assimilated into ERA40.

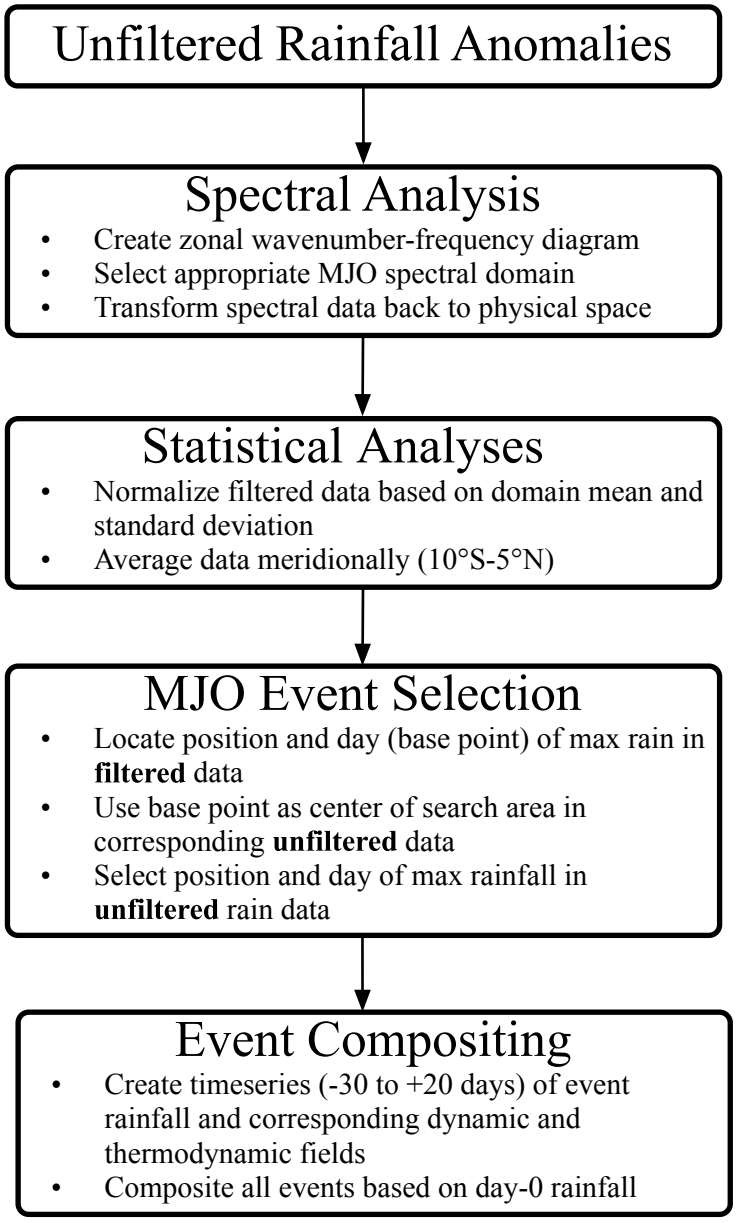


Fig. 1. Flow diagram of MJO event selection and compositing process.

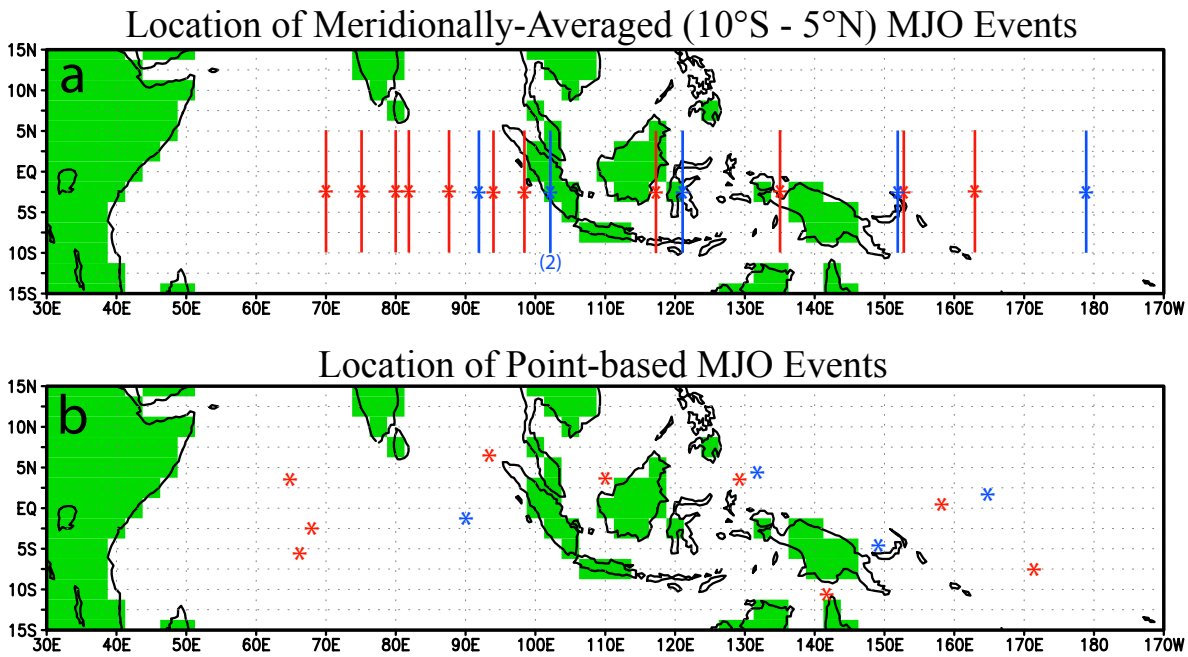


Fig. 2. (a) Map of MJO events (longitude of maximum rainfall), detected in both TRMM (red and blue) and ERA40 (red only) datasets, that make up the composite plots for the meridionally-averaged (10°S-5°N) framework. (b) As in (a) but for the individual ERA40 gridpoint cases. Green shading represents the ERA40 land-sea mask.

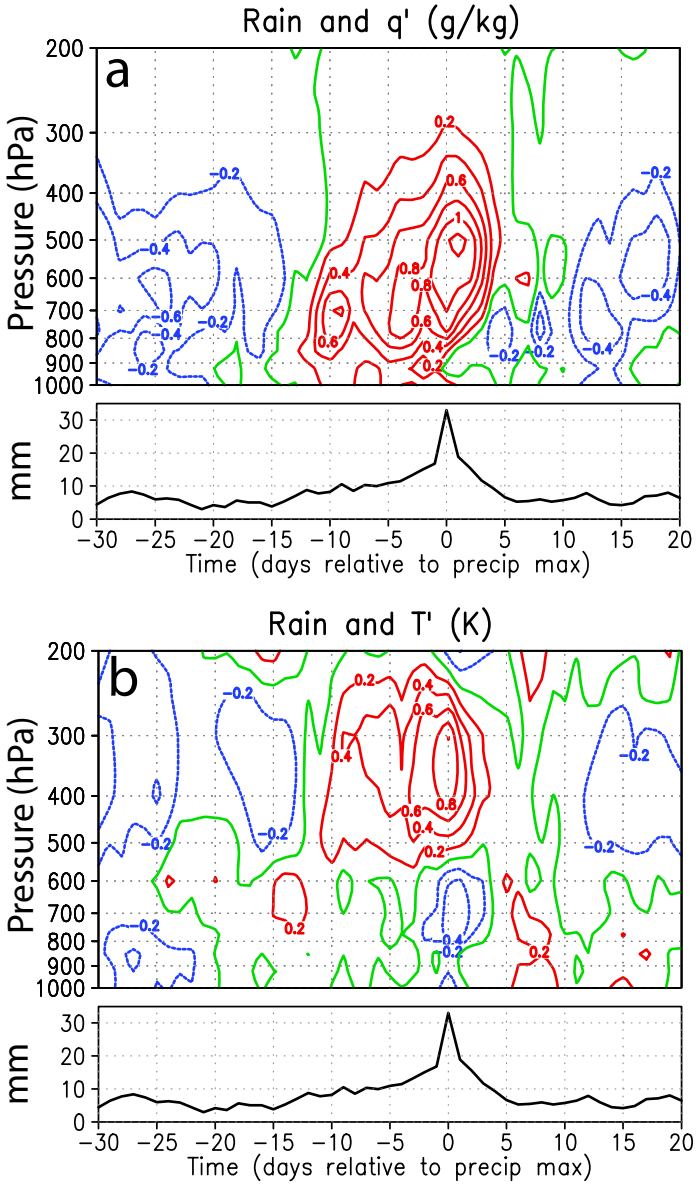


Fig. 3. Composite plots of (a) q' and (b) T' for the meridional average framework. The corresponding composite TRMM rainfall timeseries is plotted below both panels. Solid red lines (dashed blue, solid green) are positive (negative, zero) departures from the MJO background state (see Appendix A). Lag days relative to maximum rain appear on the horizontal axis.

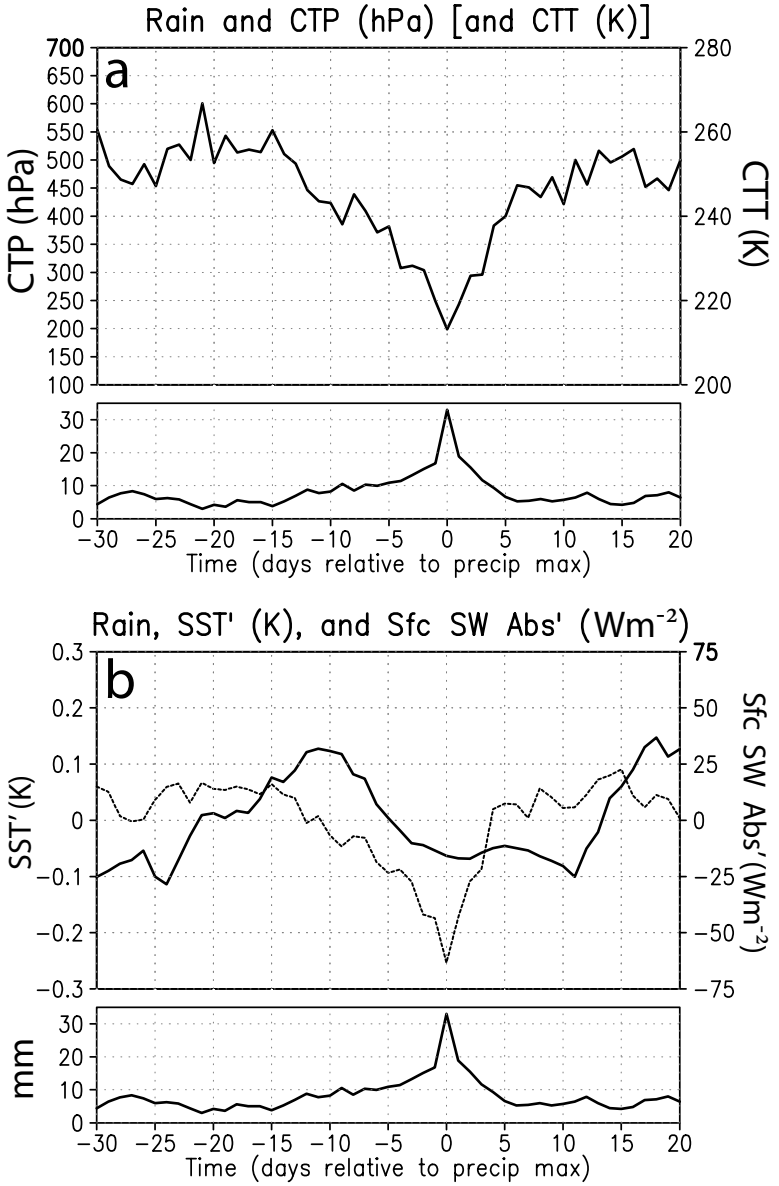


Fig. 4. (a) As is Fig. 3, but for MODIS CTP (left vertical axis) and CTT (right vertical axis). (b) As in (a) but for *SST′* (solid) and surface solar absorption (*SSA′*, dashed).

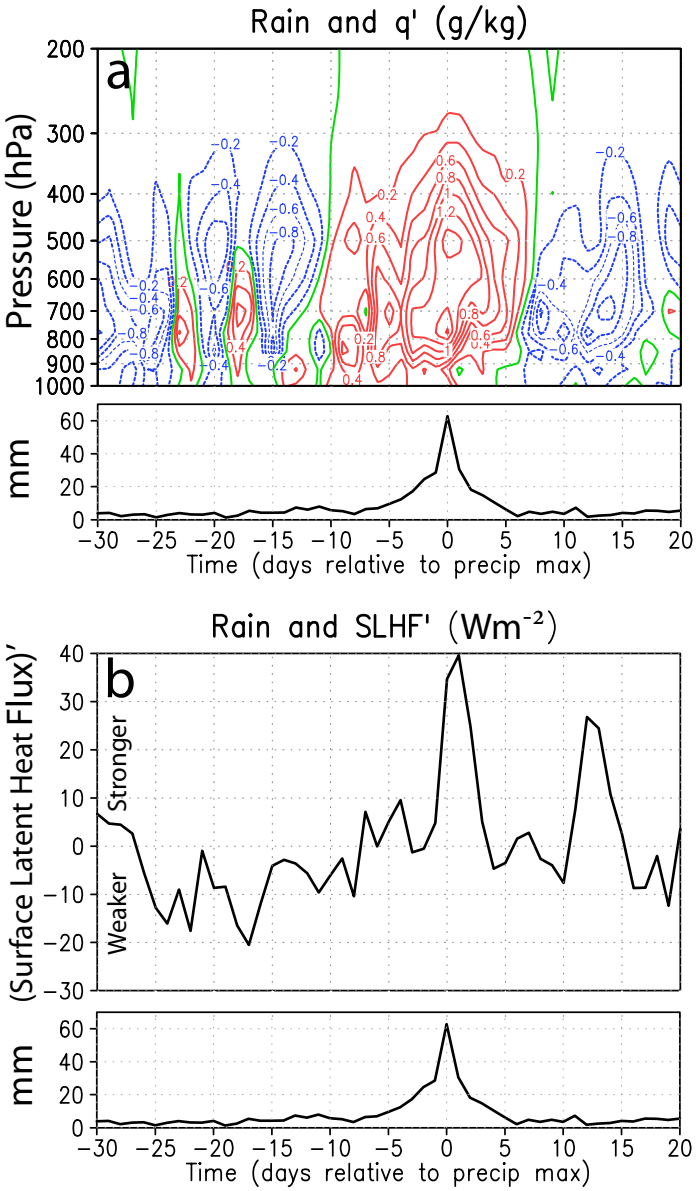


Fig. 5. As in Fig. 3 but for (a) q' and (b) $SLHF'$ for the gridpoint framework.

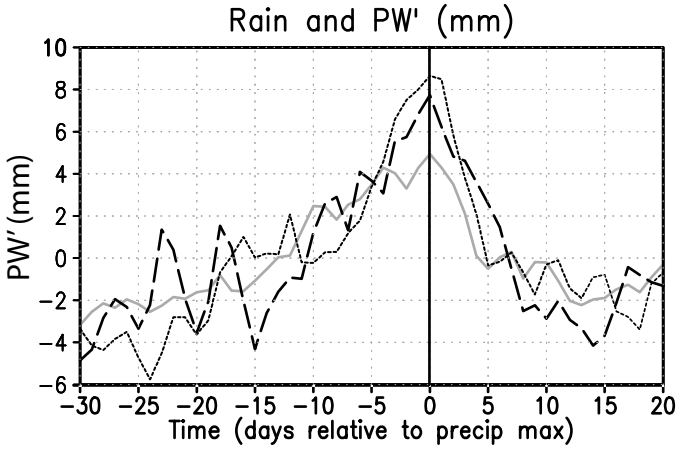


Fig. 6. As in Fig. 3 but for *PW′* based on the meridional average (solid gray), gridpoint 10-100-day filter (dotted), and gridpoint 20-100-day filter (dashed) frameworks.

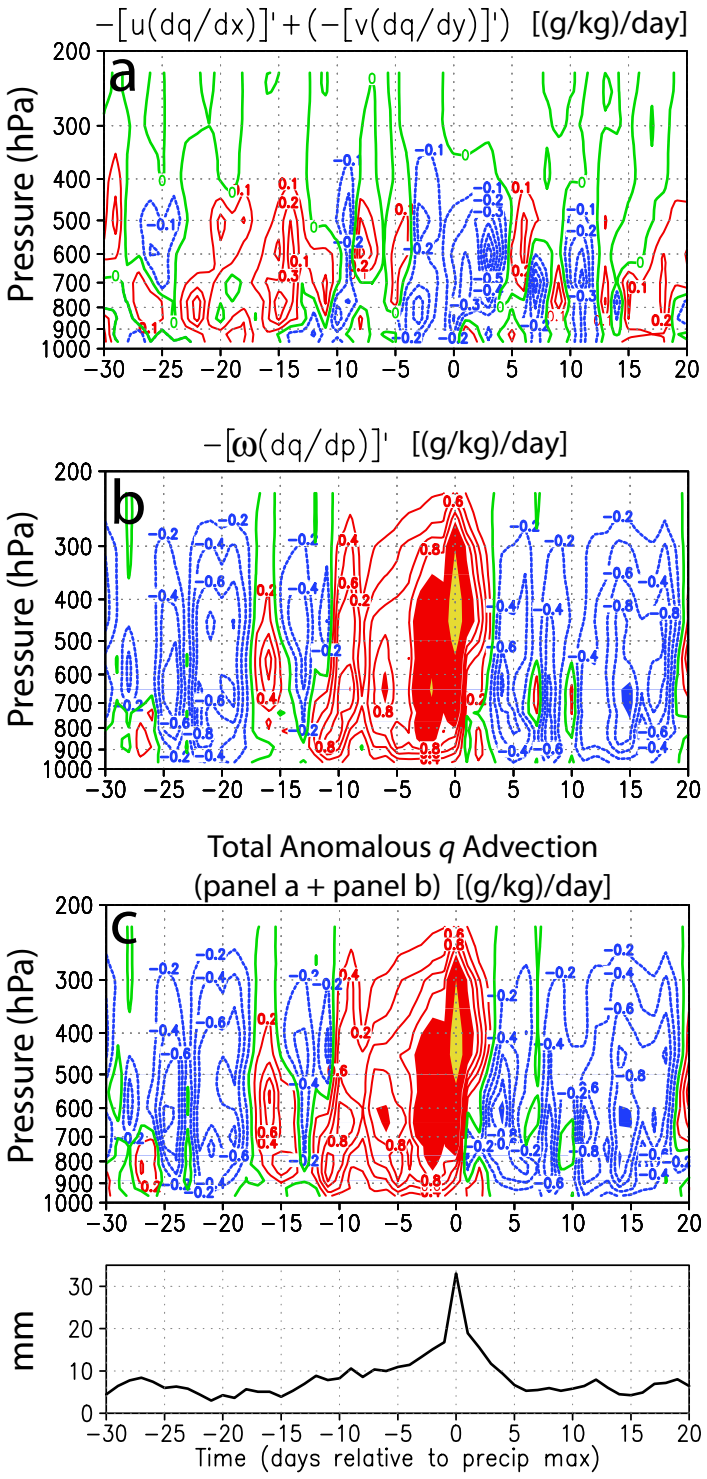


Fig. 7. Plots of the (a) horizontal, (b) vertical, and (c) combine (horizontal + vertical) composites of the $\partial q'/\partial t$ for the meridional average framework. Contour scheme is identical to Fig. 3, except that (a) is half the interval [0.1 (g/kg)/day] as (b) and (c). Blue, red, and yellow shading indicate values <–1.0 (g/kg)/day, between +1.0 and +2.0 (g/kg)/day, and >2.0 (g/kg)/day, respectively.

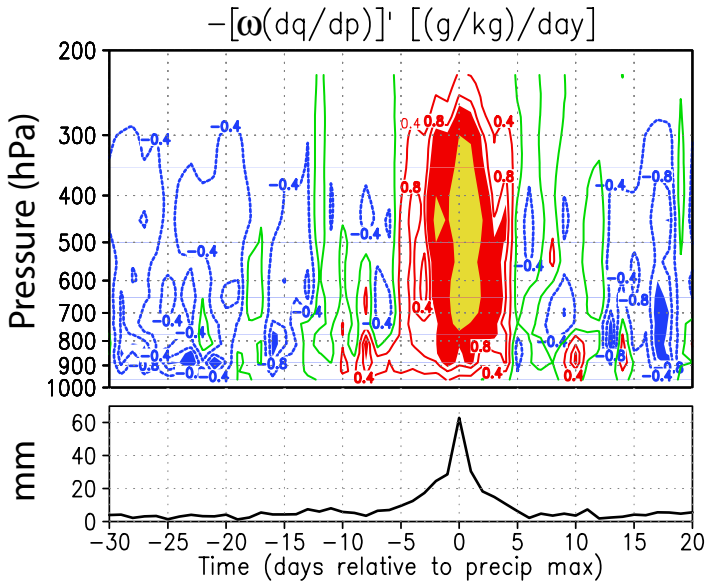


Fig. 8. Composite plot of the vertical component of $\partial q'/\partial t$ for the gridpoint framework. Contours and shading scheme are identical to those used in Fig. 7.

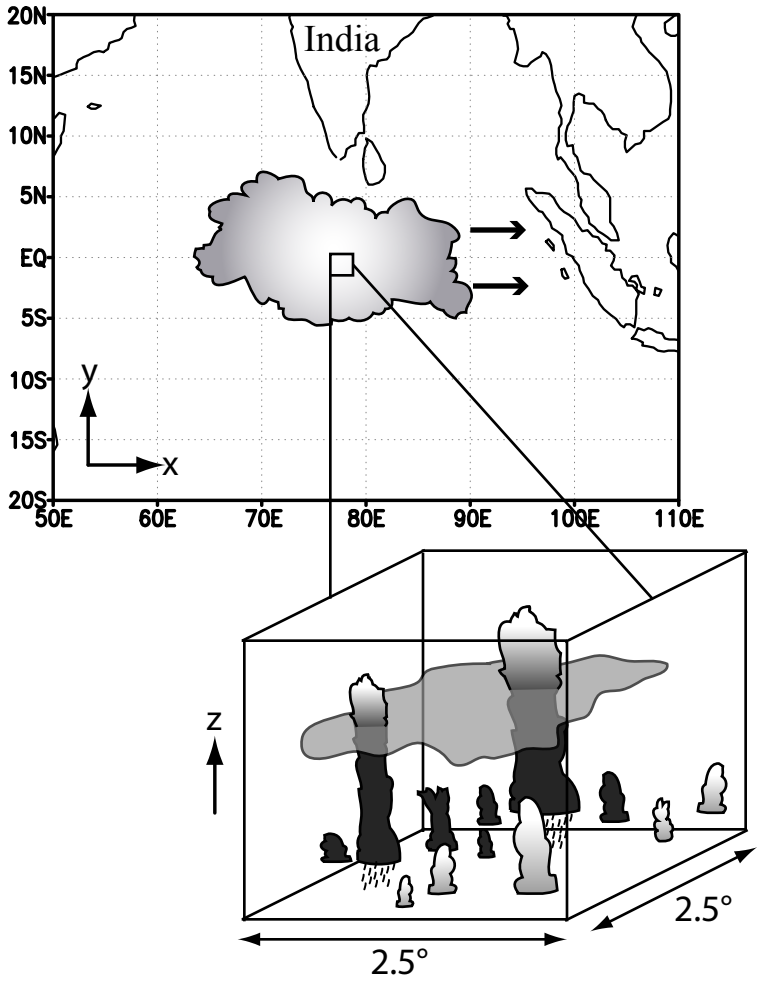


Fig. 9. Schematic diagram illustrating tropical cloud system scale differences. The x-y map depicts an eastward-propagating intraseasonal oscillation (ISO) organized on scales of O(1000 km). Within a single reanalysis grid cell (e.g., ERA40, 2.5°x2.5°), which itself constitutes a small area of the ISO, an ensemble of convective clouds exists. Deeper convective towers may be "connected" by stratiform or cirriform clouds associated with detrained moisture. A number of shallow cumuli (darker shading) are shadowed by the stratiform or anvil clouds and may not be detected by passive satellite sensors, while others (lighter shading) develop under a clear sky. Q_1' and Q_2' account for the contributions of the convective cloud ensemble to the larger-scale environment.

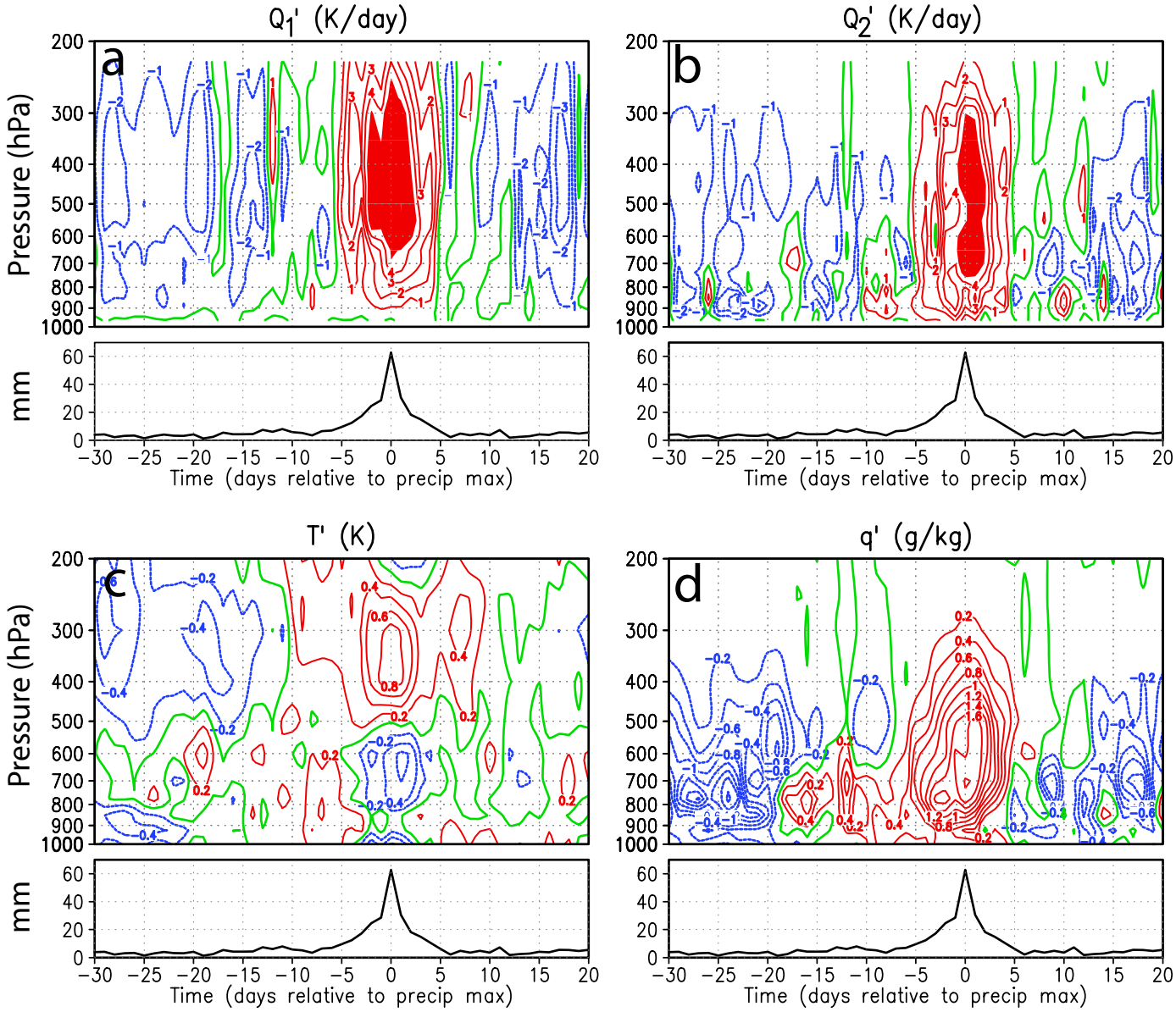


Fig. 10. Plots of (a) the apparent convective heat source Q_1', (b) apparent convective moisture sink Q_2' (positive values are associated with drying), (c) T', and (d) q' from the MJO background state (see Appendix A) for the gridpoint framework. The corresponding TRMM rainfall composite for this framework appears below each panel. The general contour scheme is identical to Fig. 3, with red shading representing values >5 K/day in panels (a) and (b).

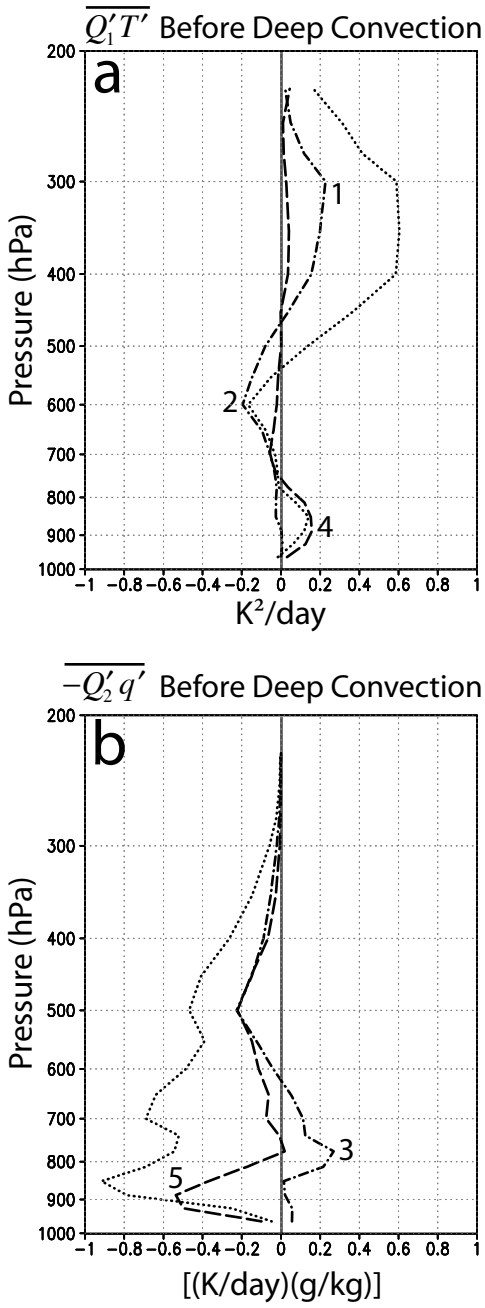


Fig. 11. Vertical profiles of (a) $\overline{Q_1'T'}$ and (b) $\overline{-Q_2'q'}$ averaged over three stages leading deep convection, for the gridpoint framework. Profiles are represented by dotted (days -30 to -15), dot-dashed (days -15 to -10), and dashed (days -10 to -5) lines. Numbers indicate features that may be discussed in the text.

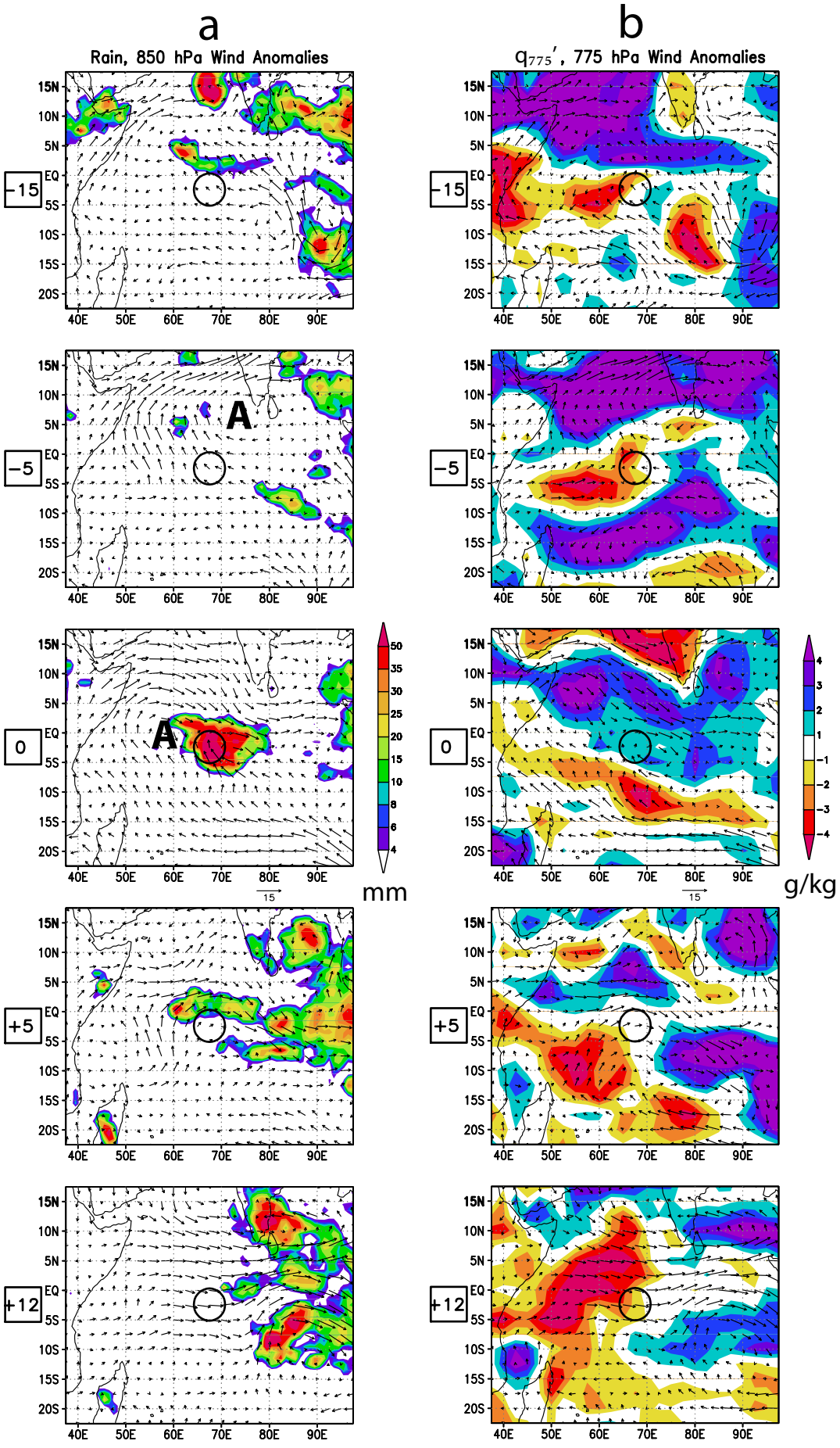


Fig. 12. Map sequences of (a) TRMM total rainfall and anomalous 850 hPa horizontal wind ($\mathbf{v}_h'$) and (b) q' and $\mathbf{v}_h'$ at 775 hPa for the event of 21 October 1998 based on the gridpoint framework. Here, anomaly values represent departures from the climatological mean (1984-2001). Lag days are to the left of each panel. Maximum wind vector and shading scale are below and to the right of the zero lag day panel, respectively. The zero lag day corresponds to the day of maximum rain at the geographical base point (2.5°S, 67.5°E, circled in each panel). Letter "A" represents an anticyclonic gyre as discussed in the text.

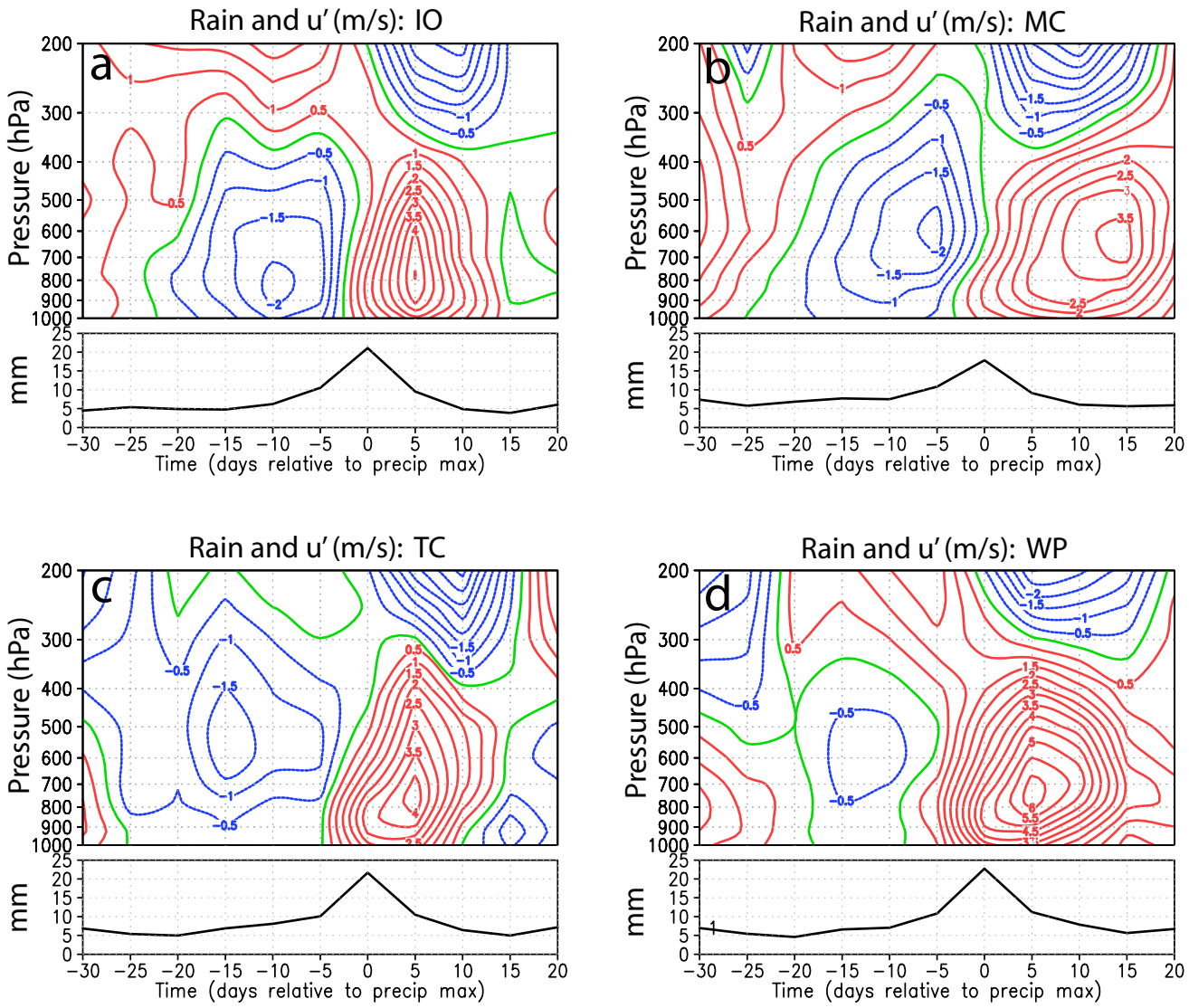


Fig. 13. Composite plots of u', based on the meridional average framework, for MJO events in (a) the Indian Ocean (IO), (b) Maritime Continent (MC), (c) TOGA COARE (TC), and (d) West Pacific (WP) regions. Corresponding TRMM precipitation profiles appear below each panel. Solid red lines (dashed blue, solid green) are positive (negative, zero) departures from climatology (1984-2002).

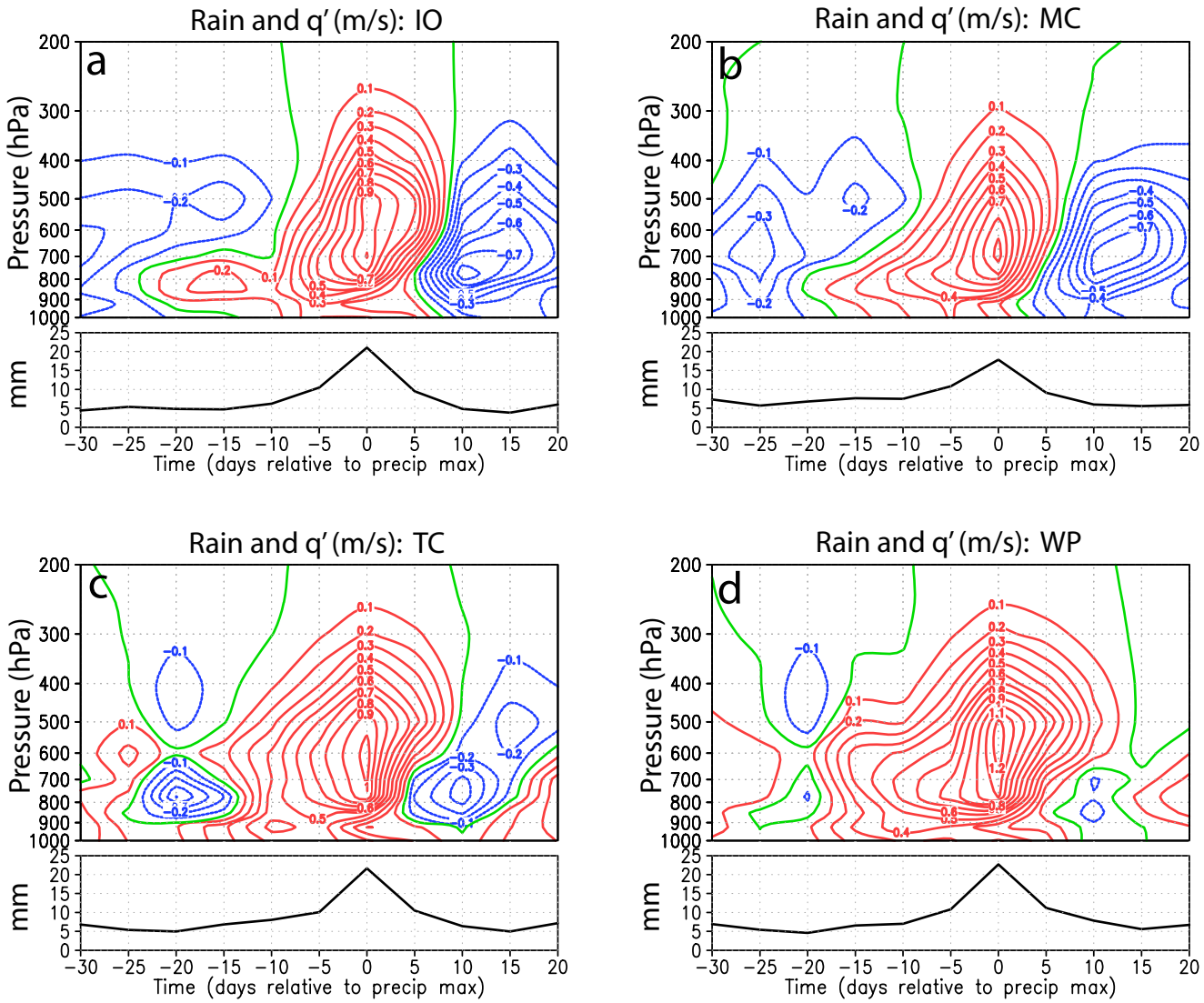


Fig. 14. As in Fig. 13 but for q'.

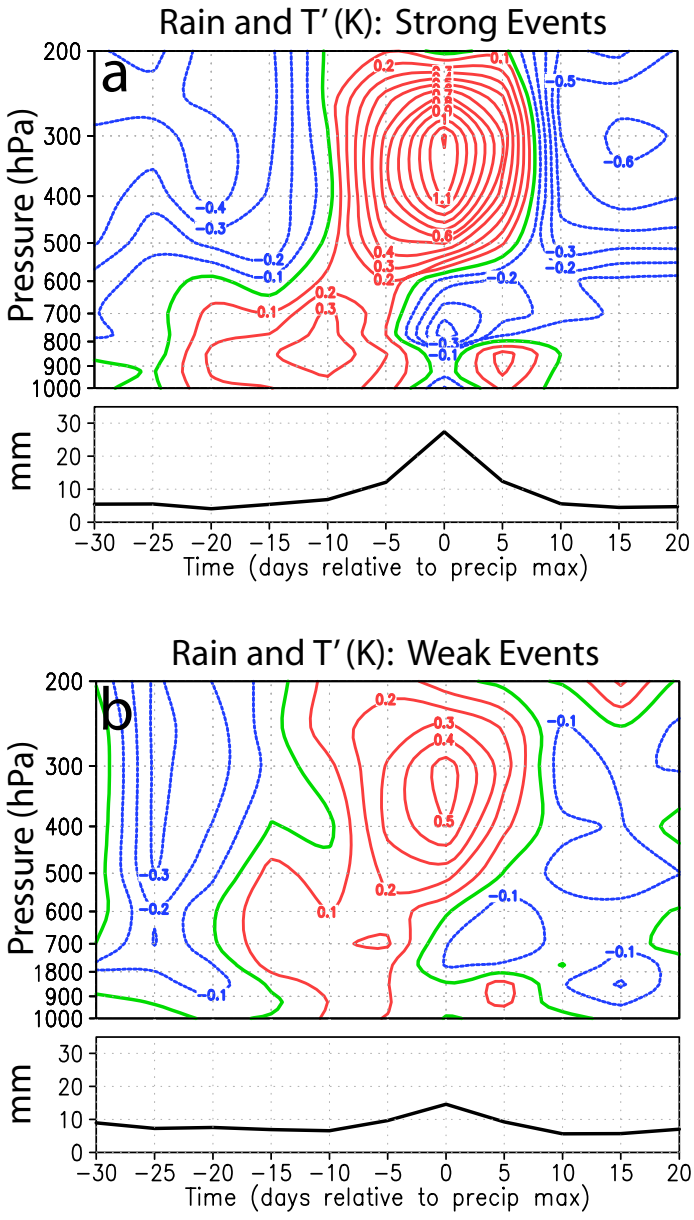


Fig. 15. Composite plotss of T', based on the meridional average framework, for MJO events classified as "strong" and "weak" (see text). Corresponding TRMM precipitation profiles appear below each panel. Solid red lines (dashed blue, solid green) are positive (negative, zero) departures from climatology (1984-2002).

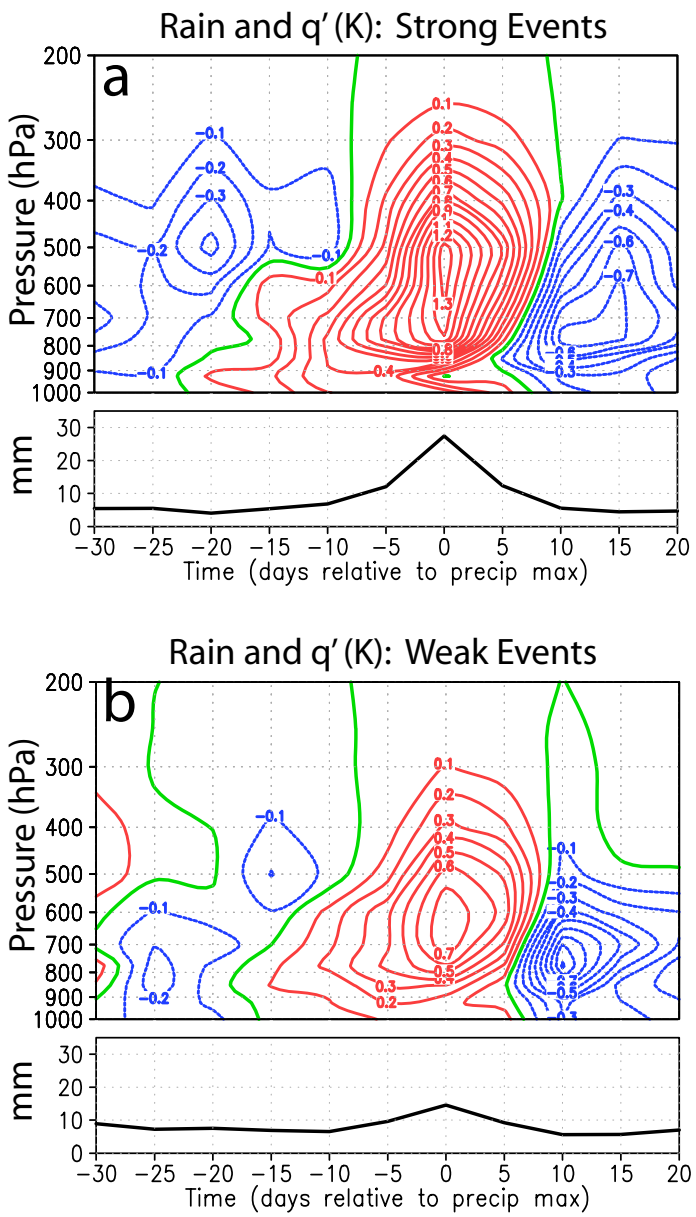


Fig. 16. As in Fig. 15 but for q'.

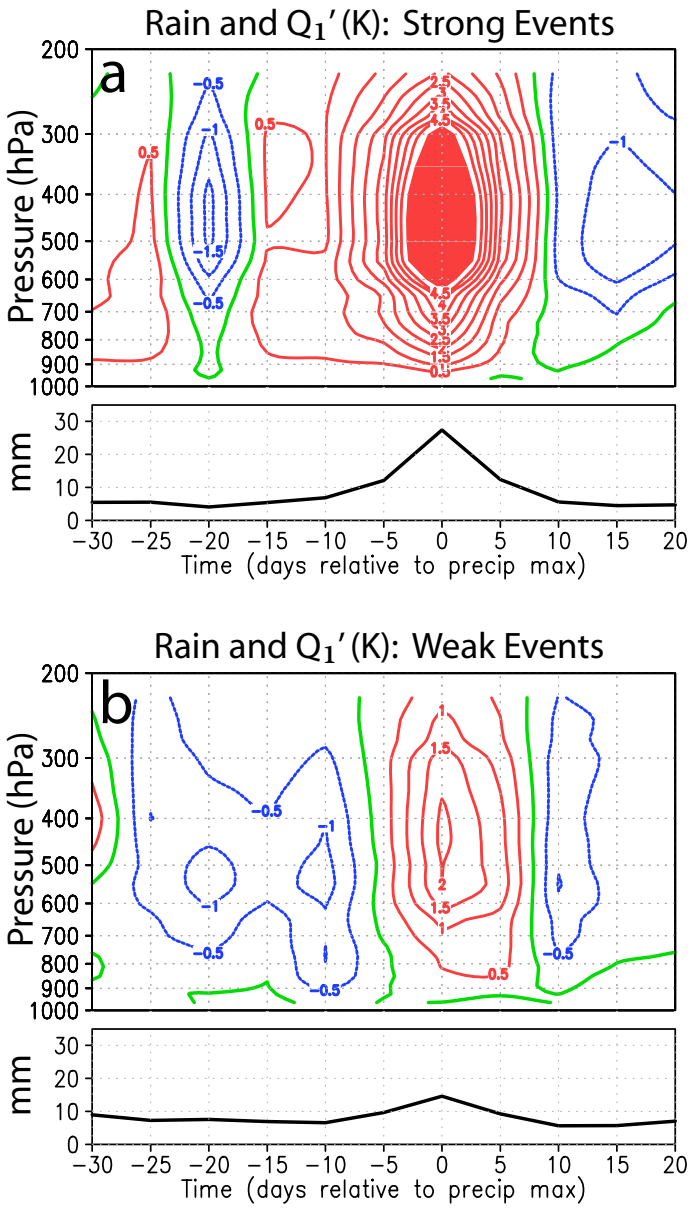


Fig. 17. As in Fig. 15 but for Q_1'. Red shading indicates heating values >5 K/day.

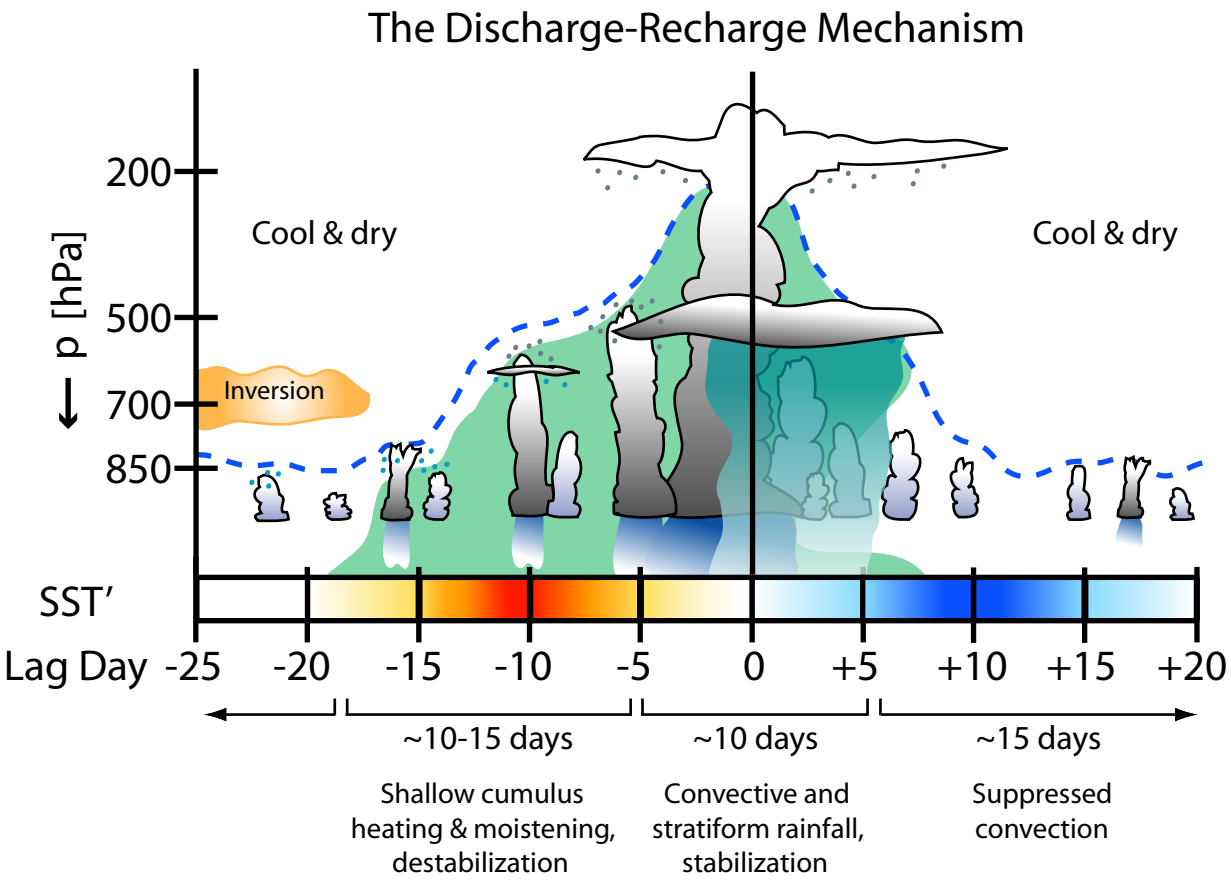


Fig. 18. Schematic diagram of the discharge-recharge mechanism associated with the MJO. Along the horizontal axis appears SST' [red (blue) indicates warmest (coolest) anomalies] and the lag days relative to the day of maximum rainfall (day 0). Approximate stages of the discharge-recharge process, as seen in ERA40 data, are listed below the lag days. The approximate top level of convective cloud processes is indicated by the dashed blue line, while green shading represents the general area of $q' > 0$. Light blue dots above shallower convective clouds represent moistening via detrainment, while gray dots below stratiform cloud types represent ice crystal fall-out and moistening. Convective precipitation is indicated by darker blue rain shafts, and stratiform precipitation are light blue and slightly transparent.

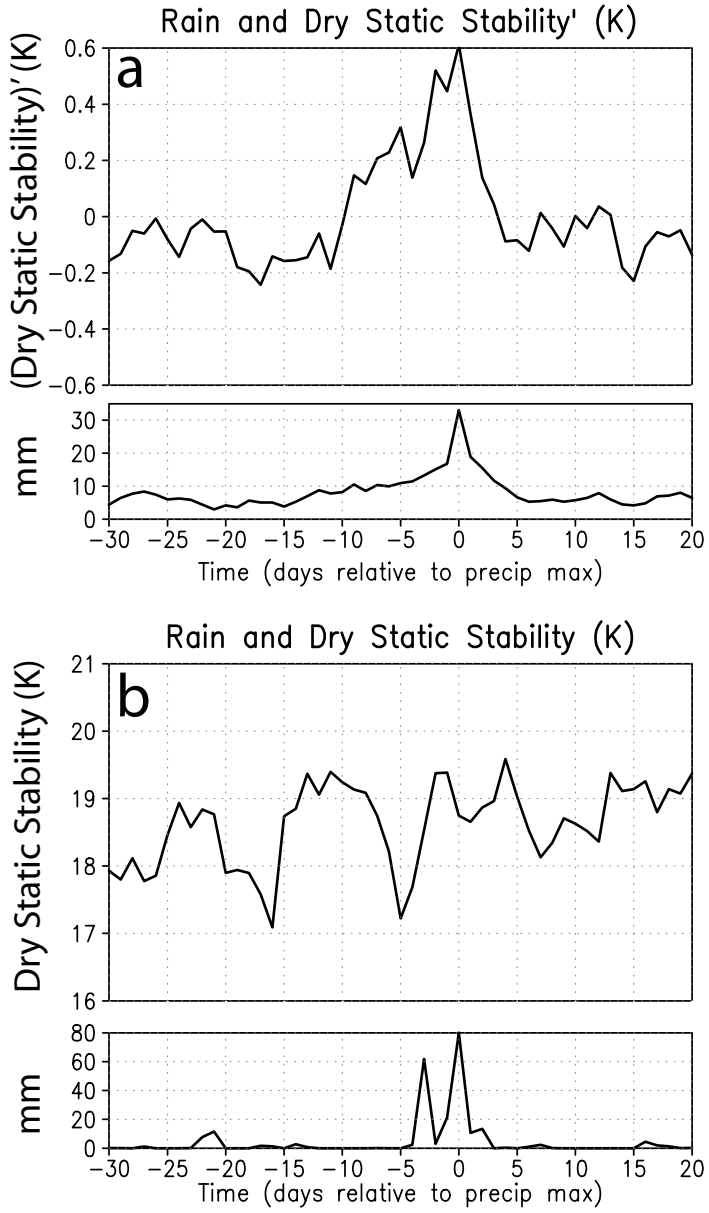


Fig. 19. Timeseries of (a) the composite departures of dry static stability (defined in text) from climatology (1984-2002) for the meridional average framework, and (b) total dry static stability for the MJO event of 21 October 1998 for the gridpoint framework. Corresponding timeseries of TRMM precipitation appear below each panel.